Prediction of Aerodynamically Induced Hood Vibration of Trailing Vehicles

THESIS

Presented in Partial Fulfillment of the Requirements for the Degree Master of Science in the Graduate School of The Ohio State University

By

Rodrigo Auza-Gutierrez, B.S.

Graduate Program in Aeronautical and Astronautical Engineering

The Ohio State University

2019

Master's Examination Committee:

Jack J. McNamara, Advisor

Austin Kimbrell

Mei Zhuang

Abstract

This thesis details aeroelastic response prediction of hoods on automobiles in the wake of a leading vehicle. Such conditions can lead to significant hood vibration due to the unsteady loads caused by vortex shedding. A primary focus is the sensitivity of the aeroelastic response to the aerodynamic modeling fidelity. This is assessed by considering both Reynolds-Averaged Navier-Stokes (RANS) and Detached Eddy Simulation (DES) flow models.

The aeroelastic analysis is carried out by coupling a commercial computational fluid dynamics (CFD) solver (StarCCM+) to a commercial computational structural dynamics (CSD) solver (Abaqus). Two different configurations are considered: 1) sedan-sedan and 2) sedan-SUV. This enables the consideration of both varied geometry and structural stiffness on the aeroelastic response. Comparisons between RANS and DES emphasize the importance of turbulence modeling fidelity in order to capture the unsteadiness of the flow and the vibration response of the hood. These comparisons include analysis of the lift forces, pressure loads on the hood, and Power Spectral Density Analysis (PSD) of the flow in the region between the two vehicles. As expected, DES predicts higher frequency content and significantly higher turbulence levels than RANS. Both the sedan and SUV hoods are sensitive to the turbulent fluctuations predicted by DES. The increased levels of turbulence result in up to 40 - 60% higher maximum peak to peak deformation and the excitation of a torsional mode of the hood for the

sedan-sedan case. For the more flexible hood configuration (sedan - SUV), these differences are even higher, with maximum peak to peak deformations of up to 17 – 71% higher than the RANS solution.

Dedication

This thesis is dedicated to my family.

Acknowledgments

I would like to express my gratitude to my academic advisor, Dr. Jack McNamara for his guidance throughout my graduate studies. His passion, dedication, and enthusiasm for research have motivated me to work as hard as I possibly can. He has not only been an immense source of technical knowledge, but also a role model inside and outside the office and classroom. I am extremely grateful to have had the opportunity to work under the guidance of a world class engineer and researcher. Additionally, I wish to thank Dr. Mei Zhuang for serving as a committee member.

I am grateful to Honda R&D Americas, Inc. for funding this project. I am thankful to have had the opportunity to work on such a great research project for a world leader in the automotive industry. Special thanks to Peter Kang for building and providing the structural models. I would like to thank Austin Kimbrell for his technical insight as well as serving as an external committee member for my master's examination. Additionally, thanks to Allen Sheldon for his support and management of this project.

I am grateful to the Simulation Innovation and Modeling Center (SIMCenter) for the computational resources. My work could have not been possible without all the resources they facilitated. Additionally, special thanks to the members of the Multi-Physics Interactions Research Group (MIRG) and

Zhenyu Wang from SIMCenter for their technical insight and discussions that helped me answer difficult research questions.

Lastly, I would like to express my immense gratitude to my family for supporting and encouraging me.

Vita

2017..... B.S. Aeronautical and Astronautical Engineering, The Ohio State University

2017 to 2018 ..... Graduate Research Associate, The Ohio State University

Fields of Study

Major Field: Aeronautical and Astronautical Engineering

Table of Contents

List of Tables

List of Figures

Chapter 1: Motivation and Objectives

1.1 Introduction

Automobile hood design is driven by many, often conflicting factors, such as: strict government regulations, customer satisfaction, fuel economy, weight, manufacturability, aerodynamic performance, aesthetics, structural integrity, and pedestrian safety standards. The pursuit for improved fuel economy and overall weight reduction drive designers to reduce the thickness of the hood and use lighter materials to achieve those goals. Additionally, safety regulations require the hood to absorb considerable energy during a crash. However, the hood needs to withstand steady and unsteady aerodynamic loads and meet tight deflection and vibration margins. The susceptibility of the hood to adverse aeroelastic response is increased as weight and thickness are reduced. Identifying inadequate structural designs early in the design stage is key for minimizing testing and manufacturing costs. This motivates the development and application of high-fidelity computational aeroelastic tools for use in the design and analysis of automobiles.

1.2 Literature Review

This section summarizes previous relevant work on the topics of automobile aeroelasticity and turbulence modeling approaches for external ground vehicle aerodynamics.

1.2.1 Automobile Aeroelasticity

Literature on the problem of automobile aeroelasticity is limited. Pesich et al. [1] investigated the response of a sedan-type vehicle hood under steady fluid loading at highway speeds. Results from this investigation indicated that underhood pressure and flow through the front and rear fascia have a moderate impact on the displacement prediction. Additionally, this investigation revealed some sources of discrepancy between experiments and uncoupled displacement prediction. Overall, the aeroelastic predictions and experimental results showed reasonable agreements. Transverse displacements of 1 mm or less suggested weak aeroelastic interactions for that specific vehicle. In [2], Aeroelastic simulations were carried out by Ratzel et al. to optimize the design of a flexible flap at the rear end of a passenger car. Thirteen different designs were considered, with the best attaining a 60% reduction in maximum deflection. Similarly, Massegur et al. [3] investigated the fluid structure interaction of the rear spoiler of an Indy car to optimize performance for both maneuvering and high speeds conditions. Results indicated a 3% reduction in drag while maintaining the same down force. These improvements led to a 1 km/hr increase in the top speed of the automobile. In [4], Patil et al. predicted the deflection of a flexible chin spoiler under aerodynamic loads to assess

the changes in the overall vehicle drag. The flexible chin spoiler configuration resulted in an increase in drag coefficient of 0.004, corresponding to 0.15 mile per gallon decrease in fuel economy for that specific vehicle. Results from that study agreed with experimental studies and demonstrated the value of aeroelastic predictions early in the design phase to reduce design time and eliminate re-tooling costs of flexible parts of vehicles. Gaylard et al. [5] and Gupta et al. [6] studied a one-way CFD-CSD simulation approach to predict automobile hood response under different transient onset flow conditions representative of typical driving scenarios. The results indicated large vibratory response when the vortex shedding frequency from a leading vehicle was close to natural frequencies of the hood.

While these studies focus on important aspects of automobile FSI, there are certain gaps in this body of work that motivate the need to study the unsteady aeroelastic response of automobile hoods subject to turbulent flows. For instance, the majority investigated the steady state aeroelastic response of automobile components [1-4]. Furthermore, only a limited number of studies have focused on the vibratory response of automobile hoods subject to unsteady aerodynamic loads [5,6]. In addition, these studies used a one-way coupled approach in which the aerodynamic loads are computed through rigid CFD simulation and then subsequently applied to the structure to predict the vibratory response.

1.2.2 Turbulence Modeling for External Aerodynamics of Ground Vehicles

This research is focused on the open concern of the fidelity required in modeling turbulence for accurately capturing transmission of wake induced loads to an automobile hood of a trailing vehicle. Important considerations are the dissipation of energy and the spectral content captured with different modeling approaches. To this effect, this work specifically investigates both RANS and DES level modeling. As stated before, studies on ground vehicles dealing with this topic are somewhat limited. One study by Ashton et al. investigated the flow around an Ahmed car body and a more detailed vehicle shape to assess the capabilities and limitations of both RANS and DES models for external automotive applications [7]. Several RANS and DES variations were investigated and compared against each other. The RANS models were unable to capture the separation region, while DES performed better in terms of force coefficients and general flow field characteristics. A similar study by Guilmineau simulated unsteady flow around an Ahmed body with a slant angle of 25 degrees [8]. Several K-Omega SST based DES models were used to predict the flow features in the separation region and immediate wake of the vehicle. Turbulent kinetic energy and time-averaged velocity profiles were compared with RANS simulations and experimental data. Results from this study indicated that DES, specifically the DES – SST model improves the prediction of the separation region behind the Ahmed body compared to RANS. Although there were still

some discrepancies with experimental results, the improvements in the prediction of the separation region by DES resulted in better total drag coefficient predictions. These studies demonstrate that DES turbulent models perform better than RANS in the prediction of unsteady flow behavior. However, there is no available literature that focuses on assessing the impact of turbulence modeling on the structural response prediction of automobile components.

1.3 Objectives of this Thesis

The motivation behind this study is the need to improve the understanding of the underlying physics of the problem of automobile hood aeroelasticity. The goal of this thesis is to implement a coupled Computational Fluid-Structure Interaction (CFSI) simulation framework to predict the dynamic aeroelastic response of automobile hoods in the wake of a leading vehicle. As noted, this work also seeks to assess the impact that turbulence modeling has on the structural response. This is done by comparing RANS and DES based predictions. Similarly, another goal of this work is to investigate the structural response sensitivity in high speed and turbulence conditions of a sedan and SUV hood, respectively. Lastly, the differences between fully coupled FSI and rigid CFD for the prediction of wake induced loads are examined.

1.4 Key Novel Contributions of this Thesis

The main novel contribution of this work is the implementation of a high fidelity predictive tool to conduct fully coupled FSI simulations on full-scale, 2-vechicle configurations to better understand the vibratory hood response in high speed and

turbulence conditions. Moreover, a DES turbulence modeling approach was successfully employed. Through sensitivity studies and comparisons of both flow and structural responses, DES exhibited significant increases in terms of spectral content in the flow and magnitude of wake induced loads that resulted in overall increased structural responses, while keeping a relatively similar computational cost to RANS.

Chapter 2: FSI Coupling, Governing Equations, and Overview of Turbulence Modeling

This chapter provides a description of the coupling procedure for the coupled fluid-structural analysis and the governing equations for the fluid and structural dynamics.

2.1 Overview of Fluid-Structure Interaction and Coupling Procedure

Fluid Structure Interaction is a complex physical phenomenon that is present in many fields such as aerospace, marine, biomedical, automotive, and others. It is a coupling that occurs between a deformable structure and a surrounding or internal fluid. Physically, the fluid exerts pressure loads on the structure, causing it to deform. This deformation is essentially a new effective shape over which the fluid is traveling. The new shape of the structure alters the flow patterns around it. Mathematically, the fluid and structure are governed by separate partial differential equations that are coupled through their mutually dependent boundary conditions.

FSI can be split into two main categories, static and dynamic FSI. The static problem arises when aerodynamic and elastic forces are coupled. This case is associated with the interaction between the structure and aerodynamic forces that cause elastic deformation. Dynamic FSI is the coupling between aerodynamic, elastic, and inertial forces. In this case, the aerodynamic forces can cause structural vibrations that are either stable or unstable over time.

There are two main numerical FSI coupling techniques, partitioned and monolithic. The monolithic approach solves the governing equations for the fluid and structure simultaneously with a single solver. In this method, all the equations are converged simultaneously each time step through iterations. This approach is more stable and robust than the partitioned method. However, the disadvantage of this method is that it requires a fully integrated FSI solver. In contrast, a partitioned solver uses separate fluid and structural solvers and staggers the exchange of boundary conditions. Partitioned solvers are either loosely or strongly coupled. Strongly coupled partitioned solvers use sub-iterations between the fluid and structural solvers between each physical time step to mitigate non-physical work imbalances that arise due to staggered time marching. Loosely coupled partitioned solvers are sub-iteration free approaches that mitigate work imbalances through carefully designed fluid and structural time integration approaches and staggering schedule. Loosely coupled solvers require less computational time, but can lead to inaccurate response predictions if not implemented properly. In this study, a loosely coupled partitioned approach is implemented. The co-simulation time marching sequence is set so that the structural solver led, and the fluid solver lagged, as shown in Figure 1. The initial solution of the co-simulation is obtained by running a flow simulation with the structural solver off. This is done to remove startup flow transients and establish realistic flow conditions over the entire domain, and especially over the hood. Inner iterations are used to converge the

fluid between each time step. The time step used in this study is set to $\Delta t = 5x10^{-4}$ seconds, and it is kept the same for both the fluid and the structure.

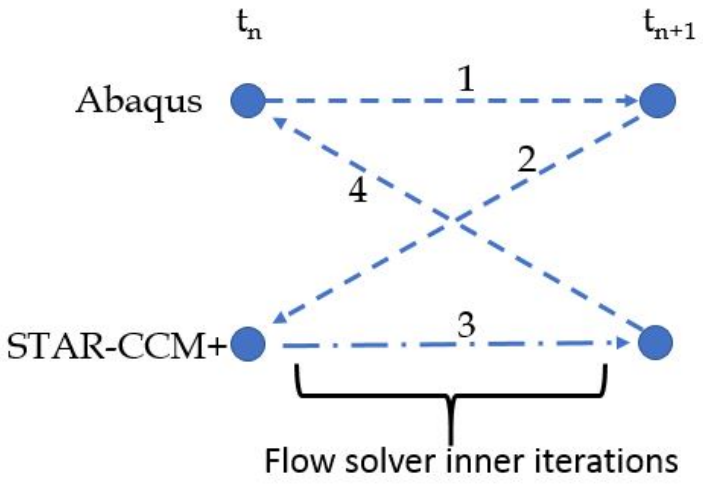

Figure 1: Co-simulation time marching sequence

StarCCM+ and Abaqus are chosen to solve the fluid and structural equations, respectively. The two solvers are coupled using the SIMULIA Co-Simulation Engine (CSE). The coupling procedure is shown in Figure 2. The fluid equations are solved first, then, the computed static pressure is mapped onto the CSD mesh as a pressure load. The structural solver computes the displacement field and then maps it back to the CFD mesh using the elemental shape functions of the finite element model. Lastly, the CFD mesh is deformed using a multiquadratic-biharmonic method, and a new hood shape is defined. This iterative process is repeated for several time steps until the desired simulation time is reached.

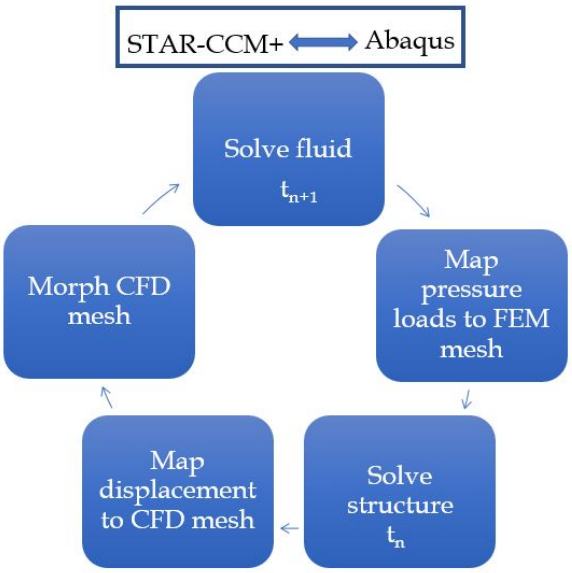

Figure 2: Co-simulation coupling procedure

2.2 Governing Equations

Next, a brief description of the governing equations that describe the fluid and structural systems is presented.

2.2.1 Fluid Flow

The fluid behavior is modeled by solving unsteady three-dimensional incompressible Navier-Stokes equations that describe the mass and momentum conservation laws, given by Equations 1 and 2, respectively:

$$\nabla \cdot \boldsymbol{u} = 0 \qquad (1)$$

$$\frac{D\boldsymbol{u}}{Dt} = -\frac{1}{\rho}\nabla p + \nu \nabla^2 \boldsymbol{u} \qquad (2)$$

where $\boldsymbol{u}$ is the velocity vector, p is the pressure and ν is the kinematic viscosity of the fluid.

2.2.1 Structural Dynamics

The general equation of motion of an elastic structure can be represented in matrix form as:

$$\mathbf{M}\ddot{\mathrm{X}} + \mathbf{C}\dot{\mathrm{X}} + \mathbf{K}\mathrm{X} = F_S(\mathrm{t}) \qquad (3)$$

where **M**, **C**, and **K** are the mass, damping and stiffness matrices, and $\ddot{\mathrm{X}}, \dot{\mathrm{X}}, \mathrm{X}$ are the acceleration, velocity, and displacement vectors, respectively. $F_S(t)$ is a transient load vector on the structure. In an aeroelastic system, F(t) is the transient aerodynamic load. Note that this matrix representation is the discrete form of the governing equation for a structural system.

2.3 Turbulence Modeling

In turbulent flows, the pressure and velocity fluctuate chaotically in both space and time. These fluctuations are characterized by a wide range of temporal and spatial scales. Resolving such a wide spectrum of scales and frequencies comes at an excessive computational cost, and it is not feasible for most engineering applications. Instead of solving the exact equations by using a Direct Numerical Simulation (DNS) approach, turbulence models are applied to solve for the averaged or filtered quantities and approximate the small scale fluctuations in the flow [10].

StarCCM+ provides several turbulent modeling options. Their applicability and fidelity depend on the problem under consideration, computational resources, boundary conditions, and spatial and temporal resolution. RANS approaches express the instantaneous governing equations in terms of the mean flow variables. RANS models

are commonly used in external aerodynamic simulations of ground vehicles. They are successful in capturing important flow features around the vehicle. However, the accuracy of such models degrades in the wake of the vehicle [7-8]. Another method to predict unsteady turbulent flows is Large Eddy Simulation (LES). This modeling approach resolves the largest scales in the flow and models the small-scale motions using a sub-grid scale model. A detailed description of sub-grid scale models in LES is presented in [9]. Although LES is a useful and accurate approach to predict turbulence, it comes at an excessive computational expense that is impractical for large scale, high Reynolds number flows due to its high grid resolution requirements. An alternative method is Detached Eddy Simulation (DES). This modeling technique is a hybrid RANS-LES approach that resolves the large turbulent scales and models the small and lower energy scales. The concept of DES turbulence modeling is based on solving the governing equations using a RANS approach near irrotational and attached wall regions and switching to LES in the unsteady and separated regions, where the turbulent eddy scales are larger than the grid size. A visual representation of DES is shown in Figure 3. DES is a suitable approach in industrial type problems, where the grid resolution and computational time need to be relatively low compared to academic type problems. A description of the specific turbulent models used in this study is presented next.

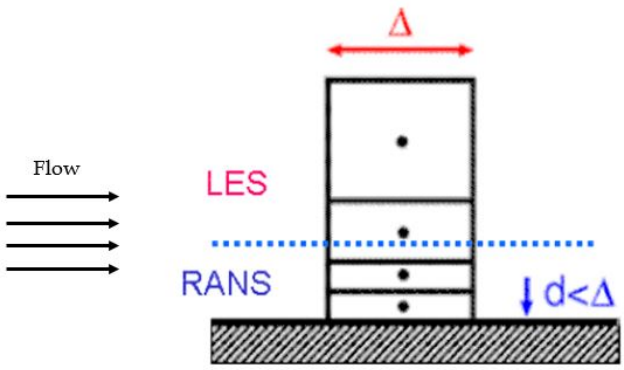

Figure 3: Visual representation of DES

2.3.1 Realizable *k*-ε RANS Model

In this study, the Realizable *k*-ε turbulent model is used. This model solves for the turbulent kinetic energy *k* and the turbulent dissipation rate ε. It is a commonly used turbulence model in many industrial applications and exhibits a good tradeoff between accuracy and computational cost [10]. The Realizable *k*-ε approach allows a critical coefficient of the model to be expressed in terms of mean flow and turbulent properties instead of being held constant. This model has shown better results than the Standard K-Epsilon model [10]. The Two-Layer approach allows for an 'all y+ treatment' of the boundary layer. This wall treatment is suitable when the y+ falls in the buffer layer (1<y+<30), which commonly occurs in stagnation regions [10]. For a brief description of the wall y+, refer to Appendix A.

2.3.2 DES *k*-ω SST Model

DES generally represents a good trade-off for high Reynolds number flows due to the reasonable computational cost of RANS near wall regions, while providing the best features of LES in regions of separated and unsteady flow [9]. In this study, the SST *k*-ω Detached Eddy model is used. This model solves for the turbulent kinetic energy *k* and the specific dissipation rate ω, defined as the rate of turbulent dissipation per unit turbulent kinetic energy. The SST *k*-ω is similar to the standard *k*-ω, except that it is less sensitive to free-stream conditions and it has an additional cross-diffusion term that effectively makes the model behave similar to the *k*-ε model in the far field and *k*-ω near the wall regions. The SST *k*-ω is widely used in aerospace applications, where viscous flows are resolved, and the boundary layer is solved using turbulence models [10]. The transition between LES and RANS depends on the local measure of the grid size and the turbulent length scales.

Chapter 3: Vehicle Configurations, Computational Setup, and Structural Model

In this chapter, the fluid and structural models are described. The vehicle configurations, computational domain setup, boundary conditions, and grid generation are discussed for the fluid models. Similarly, the structural components, materials, grid size, boundary conditions, free vibration analysis, and static analysis are presented.

3.1 Fluid Model

This section describes the vehicle geometries, boundary conditions, grid generation, and grid convergence study results.

3.1.1 Vehicle configurations

The vehicle models, provided by Honda R&D Americas Inc., represent a sedan and SUV class vehicle, respectively. Both are full scale initial designs representing only the most prominent external features of the upper cabin body. Internal flow through the engine bay is neglected and the wheels and underbody are simplified. Front, bottom, and side views of both vehicles are shown in Figures 4 and 5 respectively. Results from Pesich et al. [1] indicate that the underhood internal pressure has a moderate impact on the FSI prediction. In order account for this, a pressure load that acts on the frame and bottom of the skin is applied as a boundary condition of the structural model. This pressure load was previously obtained by Honda R&D Americas, Inc. though CFD simulation of full vehicle configurations of both vehicles.

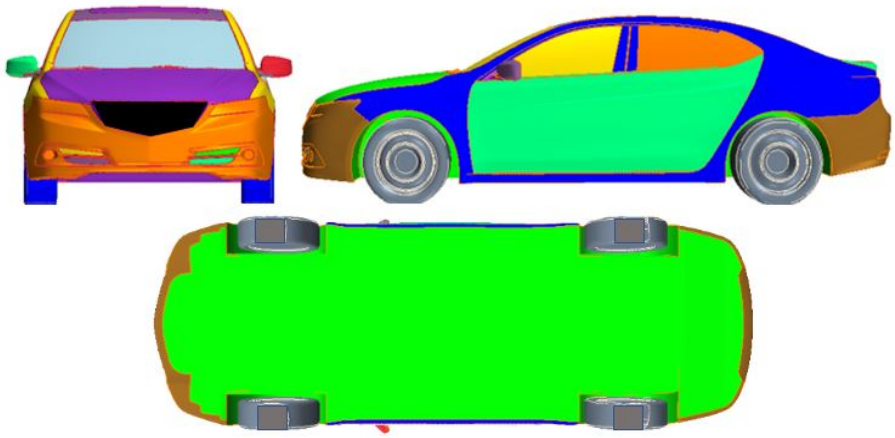

Figure 4: Sedan styling model: top, side, and bottom views

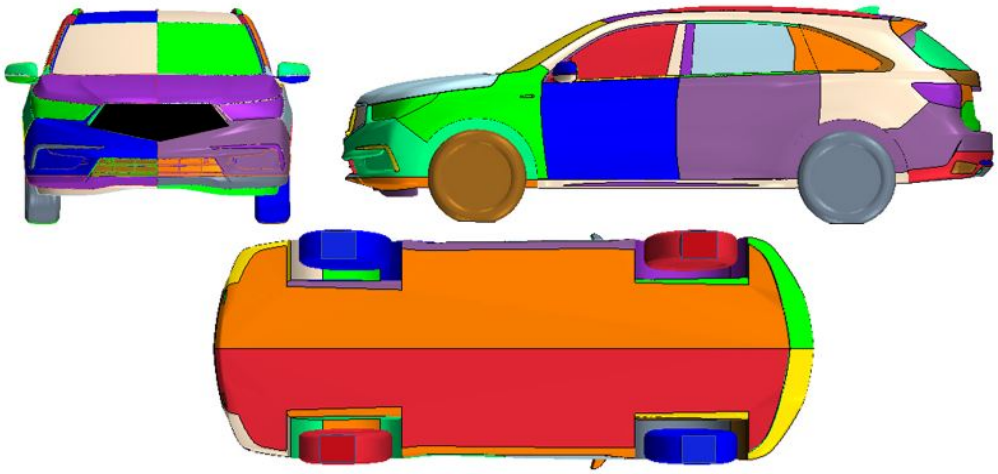

Figure 5: SUV styling model: top, side, and bottom views

3.1.2 Computational Setup and Boundary Conditions

The governing equations are discretized to second order accuracy in space and time. The time marching approach is set to an implicit scheme. The computational domains and boundary condition specifications for both configurations are shown in Figures 6-8. The vehicle surfaces are set to a no-slip condition. The inlet and outlet boundaries are set to velocity inlet and mass flow outlet, respectively. This specific outlet boundary condition allows specification of a gauge pressure at a specific location in the domain. A value of -286.976 Pa is selected based on wind tunnel experiments by Honda R&D Americas, Inc. at the same freestream velocity as the current study. The top, bottom, and side walls are specified as slip walls. The offset distance between the vehicles is 10 meters, and the free stream velocity is 200 kilometers per hour (kph), as illustrated in Figure 7.

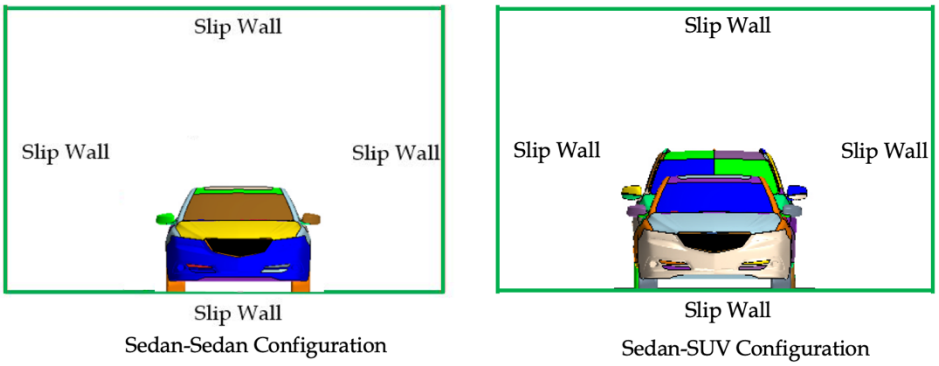

Figure 6: Front view of the computational domains and boundary conditions

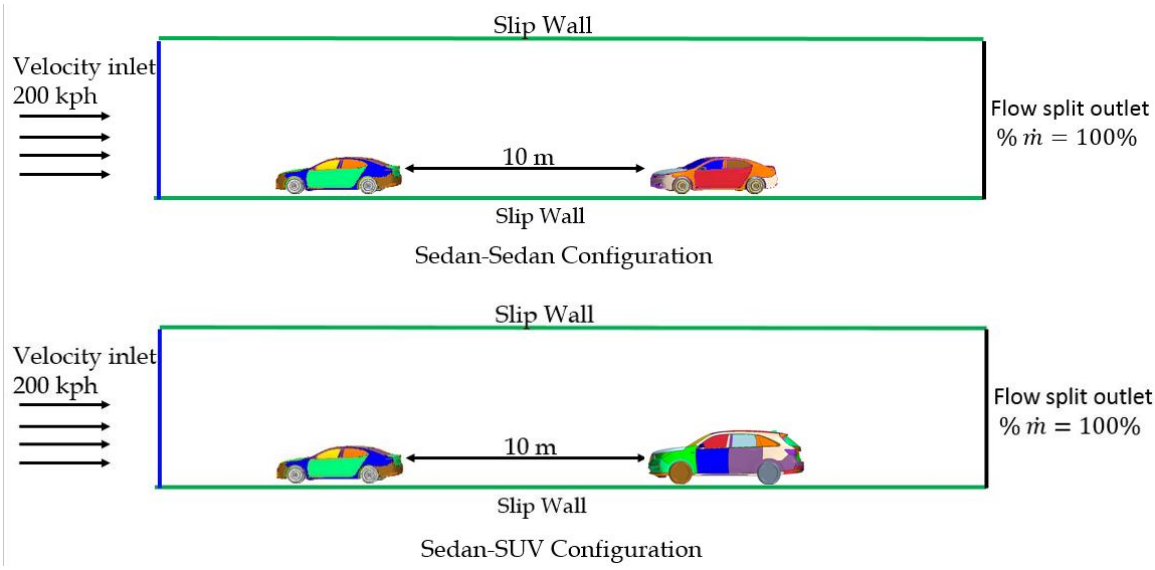

Figure 7: Side view of the computational domains and boundary conditions

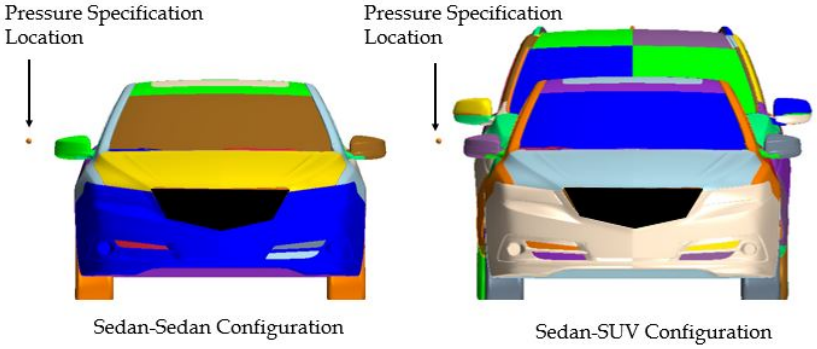

Figure 8: Gauge pressure specification location

3.1.3 Grid Generation

The grids are generated by surface wrapping the vehicle geometries. Surface wrapping is a meshing technique used to create a water-tight geometry and allows for refinement on individual surfaces based on curvature and proximity. The surfaces of the vehicles

have a surface mesh size ranging from 2.5 – 10 millimeters, depending on the complexity and region of the vehicles. The volume mesh consists of prism layers and trimmed hexahedral cells. The prism layers are extruded from the walls of the flow domain, including the vehicle surfaces, and are used to capture the boundary layer flow. The first cell height is computed so that the y+ is in the log-law range (30<y+<300). Volumetric controls for local mesh refinement are created around the vehicles and in the area between them. This is done to capture important flow features in close proximity and the wake of both vehicles. The sizes of the volumetric controls are 10 mm, 20 mm, and 40 mm, as shown in Figures 9 and 10. Additionally, side view planes of the mesh near the hood region of both the sedan and SUV are presented in Figure 11. The mesh count for both setups is listed in Table 1. Note that the cell counts of the 2-vehicle configurations presented here are approximately a factor of three times the cell count of a 1-vehicle setup presented by Pesich et al. [1], where the grid for a sedan class vehicle had 35 million cells.

Figure 9: Mesh cut plane (side) highlighting the volumetric controls

Figure 10: Mesh cut plane (top) highlighting the volumetric controls

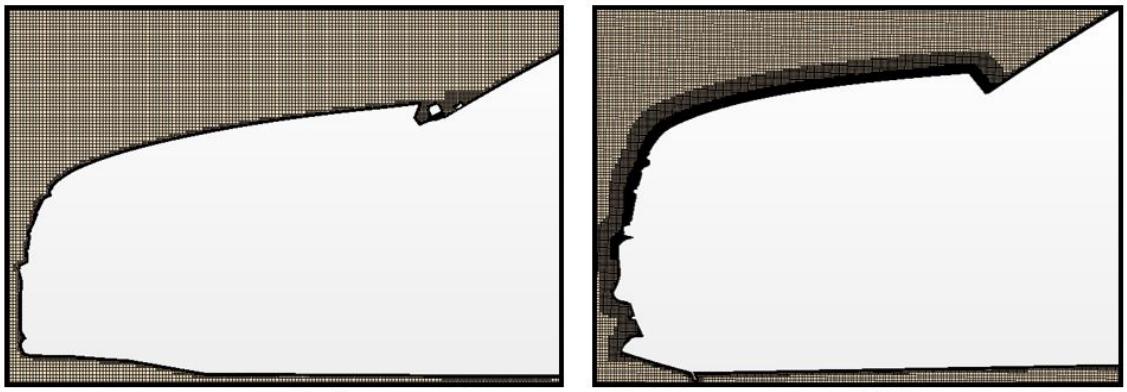

Figure 11: Sedan and SUV mesh cut plane (side) near the engine bay

Table 1: Cell count for Sedan – Sedan and Sedan – SUV configurations

Configuration	Cell Count
Sedan-Sedan	115 million
Sedan-SUV	136 million

3.1.4 Grid Convergence Study

A grid convergence study is done using the sedan-sedan configuration by comparing mean and root mean square (RMS) of the time dependent hood lift coefficient for three different grid configurations. The time averaged pressure coefficient at several discrete hood locations is also compared. Note that the time averaging of the lift and pressure coefficients is taken after a statistically stationary flow is established. This is determined to occur when the mean lift coefficient remains relatively invariant if taken at different instances in time. Furthermore, the coefficients are time averaged using 1 second of flow response after the establishment of a statistically stationary flow. The time response of the coefficient of lift during this period is shown in Figure 12. The locations of the discrete pressure strips and pressure coefficient comparisons are shown in Figures 13-18. The results for each metric are provided in Table 2.

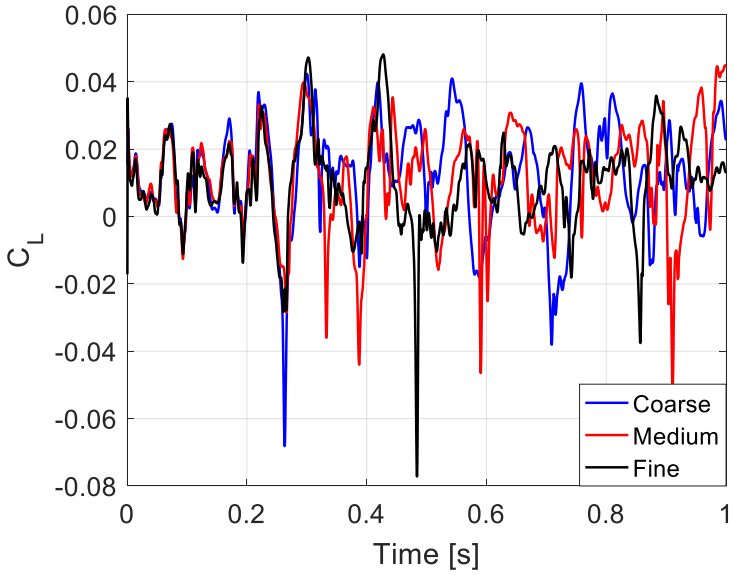

Figure 12: Time history comparison of sedan hood lift coefficient from grid convergence study

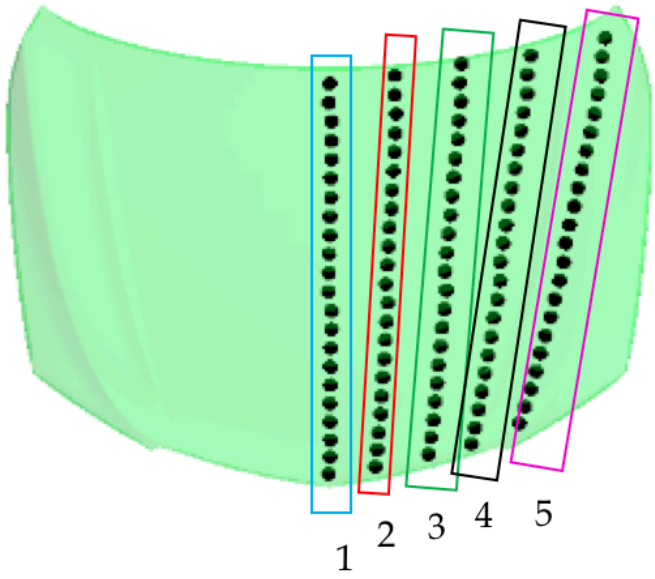

Figure 13: Discrete pressure locations for sedan hood: strips 1-5

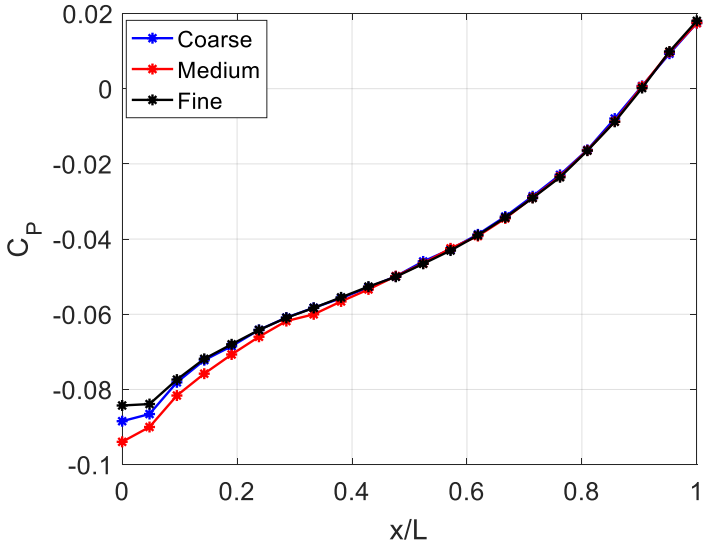

Figure 14: Time averaged pressure coefficient comparison from grid convergence study: strip 1

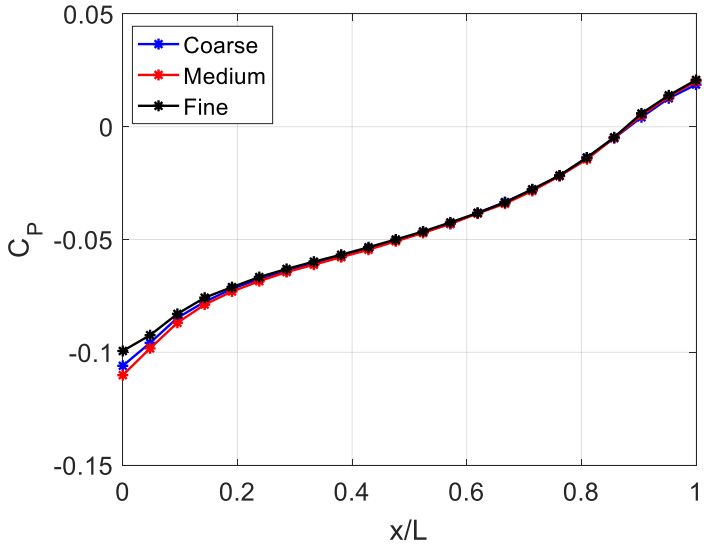

Figure 15: Time averaged pressure coefficient comparison from grid convergence study: strip 2

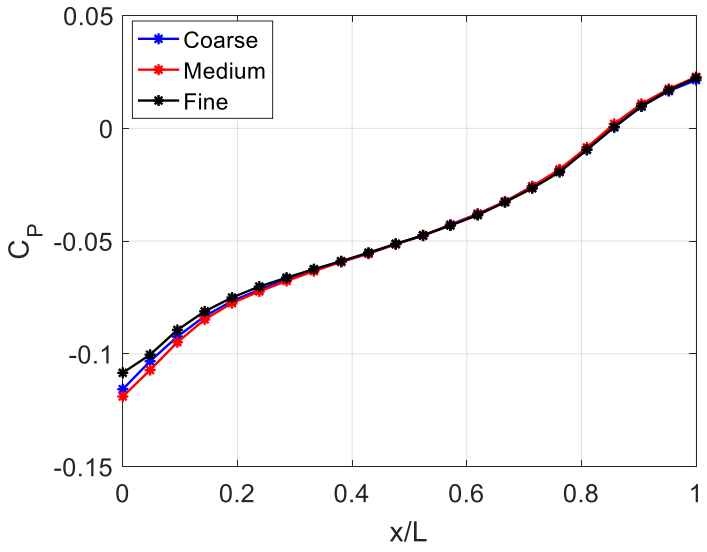

Figure 16: Time averaged pressure coefficient comparison from grid convergence study: strip 4

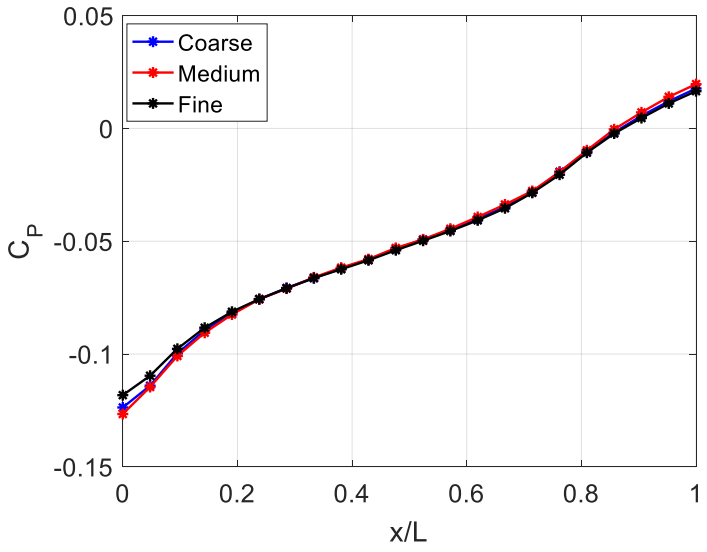

Figure 17: Time averaged pressure coefficient comparison from grid convergence study: strip 4

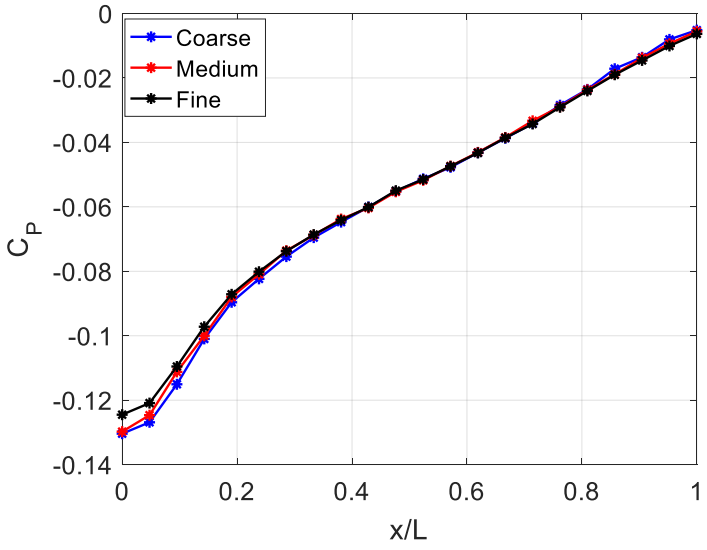

Figure 18: Time averaged pressure coefficient comparison from grid convergence study: strip 5

Table 2: Grid convergence study results: Sedan – Sedan configuration

	Cell Count	Mean C_L	RMS Fluctuating Component of C_L	RMS C_L/mean C_L
Coarse	65 million	0.0119	0.0154	1.29
Medium	115 million	0.0113	0.0151	1.34
Fine	198 million	0.0097	0.0136	1.39

These results indicate that increased grid densities are required in order to establish grid convergence. However, the results do not indicate large errors incurred by using the medium and coarse grid configurations. Thus, the medium grid configuration is chosen in order to best balance accuracy and computational requirements. Note that a similar grid configuration and density are used for the sedan-SUV configuration.

3.2 Structural Models

Honda R&D Americas, Inc. provided the Abaqus structural models for this study. The main components are the hood skin, frame, hinges, and latch, shown in Figure 19. The hood skin represents the FSI boundary subject to the pressure loads from the CFD calculations. The hood skin and frame are attached by a mastic material and the hinges and latch are bolted to the frame. The latch and hinges of the sedan model are constrained in translation but are free to rotate about any axis. For the SUV model, the hinges are constrained in all translation and rotation degrees of freedom, and the latch is only constrained in the y, z – directions. Descriptions of the components, mesh type and size, materials, and boundary conditions are listed in Tables 3-5. Note that the rotation degrees of freedom about the x,y,z axes are expressed as θ_1, θ_2, θ_3, respectively.

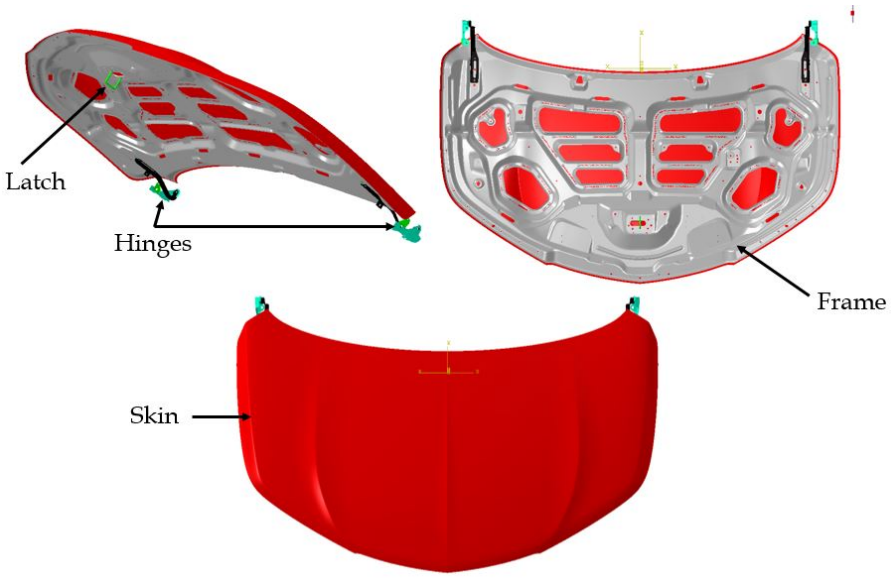

Figure 19: Main components of the structural models

Table 3 Sedan hood structural model: material and mesh description

Component	Material	Element Type	Cell Size (mm)
Skin	Aluminum	Shell	5
Frame	Aluminum	Shell	5
Hinge	Steel	Shell	5
Latch	Steel	Shell	5

Table 4: SUV hood structural model: material and mesh description

Component	Material	Element Type	Cell Size (mm)
Skin	Aluminum	Shell	2
Frame	Aluminum	Shell	2
Hinges	Steel	Shell	2
Latch	Steel	Solid	2

Table 5: Boundary conditions for sedan and SUV models

Vehicle	Component	Constrained Degree of Freedom
Sedan	Hinges	u,v,w
	Latch	u,v,w
SUV	Hinges	u,v,w,θ_1, θ_2, θ_3
	Latch	v,w

3.2.1 Free vibration analysis

The first 5 natural modes and frequencies of both hoods are listed in Tables 6 and 7. Typically, the first few modes of a structure have higher contribution to the dynamic vibration response [6]. These modes are in the 43 – 84 Hz and 13-37 Hz range for the sedan and SUV, respectively. These indicate that the SUV hood is less stiff than the sedan hood. Aerodynamic loads with strong periodicity in those frequency ranges could excite the hoods significantly.

Table 6: Free vibration analysis results for the sedan hood

Mode	Frequency (Hz)
1	43.0
2	48.5
3	61.1
4	69.7
5	83.7

Table 7: Free vibration analysis results for the SUV hood

Mode	Frequency (Hz)
1	13.1
2	20.0
3	30.5
4	30.6
5	36.6

3.2.2 Static Analysis

Further characterization of the two hoods is carried out using static analysis. One case consists of applying a 300 N/m^2 distributed lift load to the structures under the same boundary conditions as the FSI simulations. The second case consists of a sag test of the hoods under the action of gravity by constraining the hinges and the front left corner of the structure, while the rest of the hood is free to deform. Results are shown in Figures 20 and 21, respectively. Consistent with the free vibration analysis, these results indicate that the SUV hood is more compliant than the sedan hood.

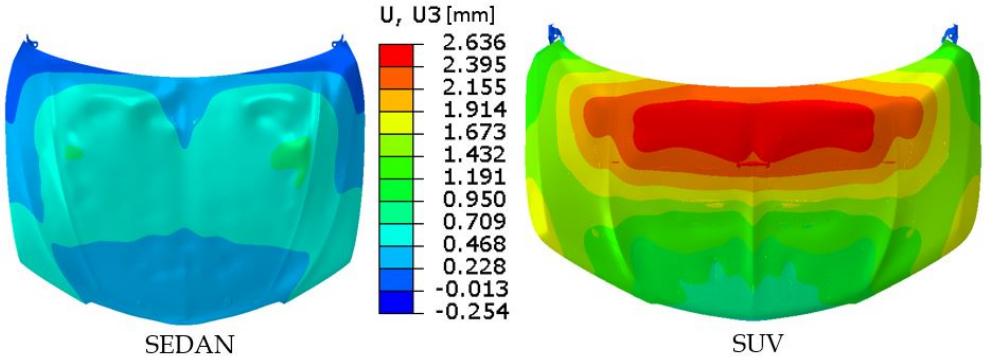

Figure 20: 300 N/m^2 distributed static load comparison

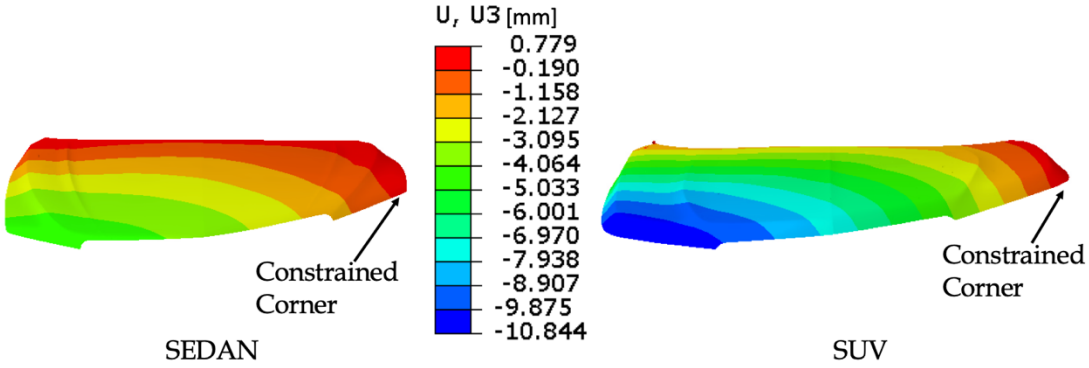

Figure 21: Gravity load comparison

Chapter 4: Results

First, flow solutions using RANS and DES are shown, including hood lift coefficient time histories, time averaged pressure coefficient distributions, and PSD analysis in the region between the two vehicles. Next, transverse displacement and instantaneous hood displacement contours are compared. Then, a discussion on the degree of aeroelastic coupling by comparing rigid versus coupled solutions is given. Last, a comparison in the computational time between rigid CFD and FSI simulations is presented.

4.1 Sedan – Sedan Configuration

In this section, the results for the sedan-sedan configuration are discussed. Flow solutions are shown initially, followed by the structural response.

4.1.1 Comparison Between RANS and DES Flow Solutions

Simulations are carried out at a free stream velocity of 200 kph for 1 second. The hood lift coefficient time history is shown in Figure 22. As expected, the DES prediction yields significantly larger and higher frequency fluctuations. From the results listed in Table 8, it is clear that while there is good agreement in the mean value for both RANS and DES, there is an order of magnitude difference in the standard deviation.

Time averaged pressure coefficient values for strips 1-5 are provided in Figures 23-27. These values are taken to localize the specific areas of the hood where the pressures differ the most. The biggest differences are seen in the leading and trailing edge regions due to the high velocity and pressure gradients in those areas. DES predicts more

negative pressure signatures towards the front end of the hood, resulting in a higher upward, or lift force. Similarly, the more positive pressures towards the back of the hood result in a larger down force.

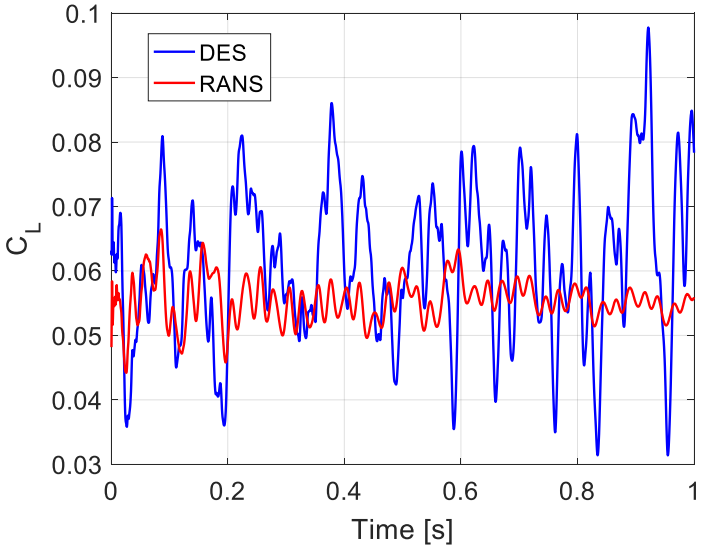

Figure 22: Time history comparison of sedan hood lift coefficient

Table 8: Mean and standard deviation comparison of sedan hood lift coefficient

	Mean C_L	Standard Deviation C_L
DES	0.0614	0.0119
RANS	0.0554	0.00326

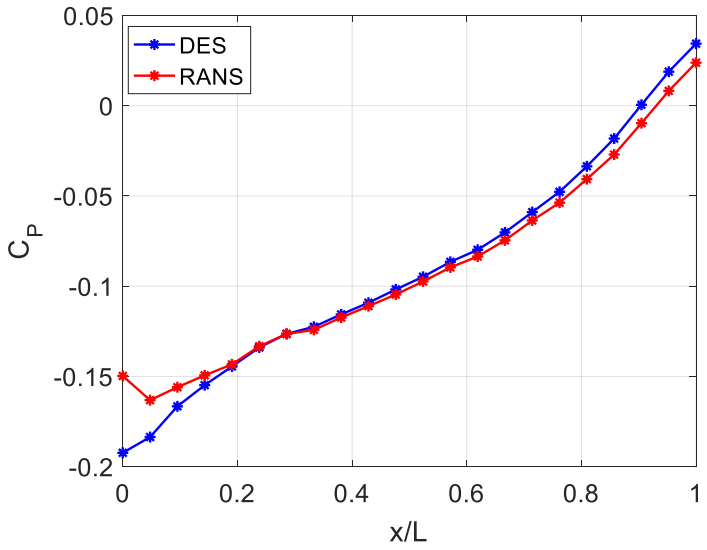

Figure 23: Time averaged pressure coefficient distribution comparison for sedan hood: strip 1

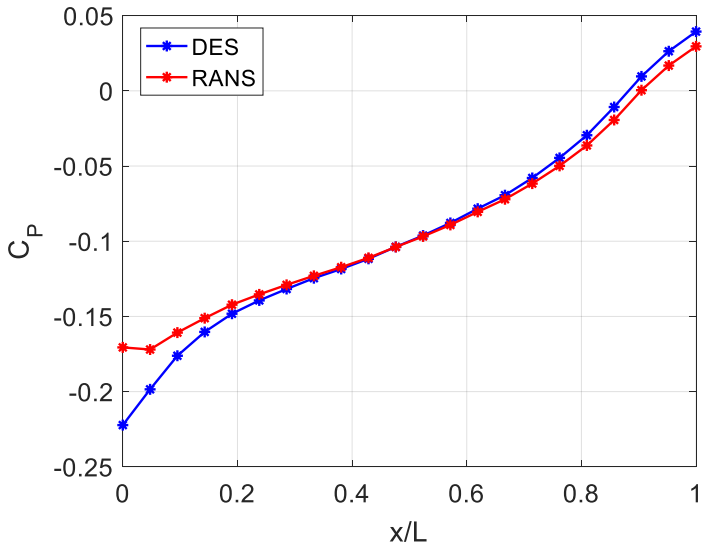

Figure 24: Time averaged pressure coefficient distribution comparison for sedan hood: strip 2

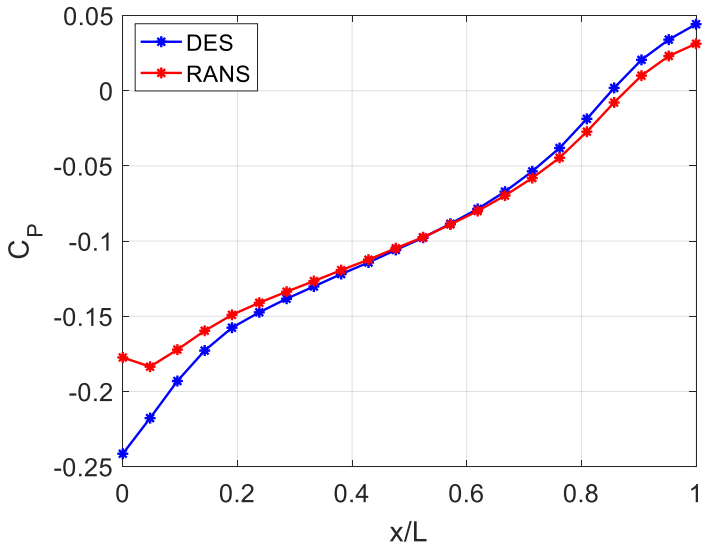

Figure 25: Time averaged pressure coefficient distribution comparison for sedan hood: strip 3

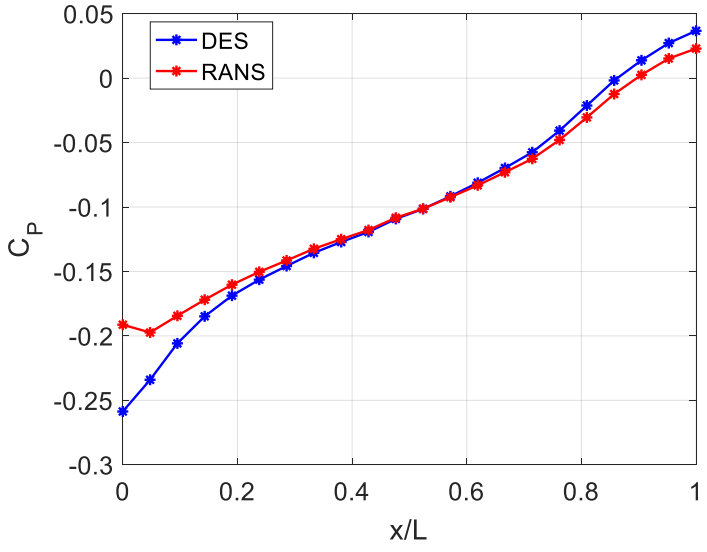

Figure 26: Time averaged pressure coefficient distribution comparison for sedan hood: strip 4

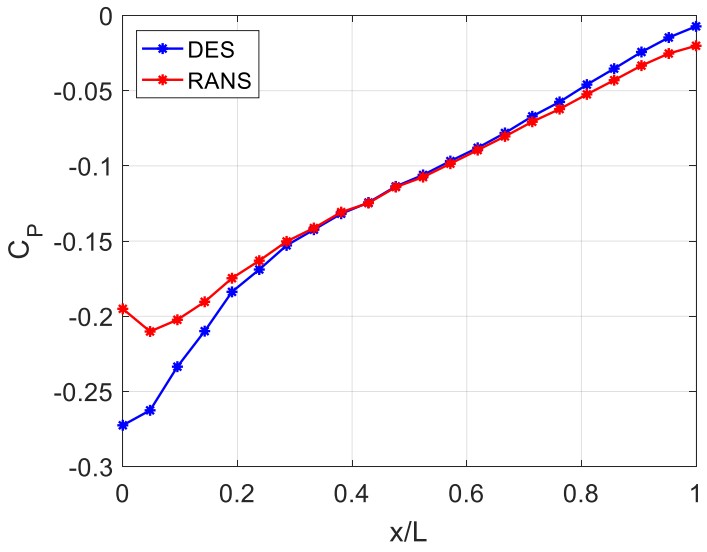

Figure 27: Time averaged pressure coefficient distribution comparison for sedan hood: strip 5

In addition to the forces on the hood, the frequency content throughout the wake is analyzed. Static pressure probes are placed in the region between the leading and trailing vehicle, illustrated in Figure 28. PSD analysis of the fluctuating component reveals the dominant frequencies of the vortex shedding and change in strength as the vortices convect downstream to the trailing vehicle.

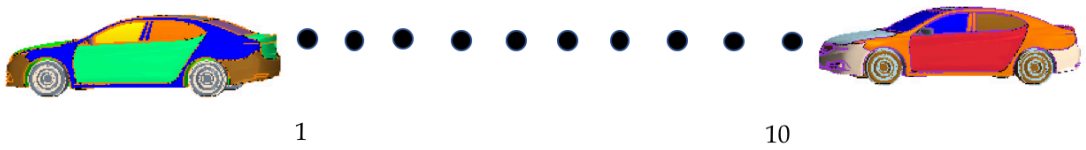

Figure 28: Static pressure probes between vehicles (sedan - sedan)

Results are shown in Figures 29-31. RANS indicates dominant frequencies between 20 - 30 Hz that dissipate quickly in magnitude downstream of the leading vehicle. In contrast, DES indicates a much broader range of frequencies and significantly less dissipation of energy as the wake convects downstream. Dominant frequencies near the trailing vehicle are between 0 - 40 Hz. Furthermore, note that the magnitude in pressure fluctuations are significantly reduced compared to DES. In particular, the fluctuation in pressure at the first probe predicted by RANS is smaller than the fluctuation predicted by DES at the last probe location. The decrease in magnitude of the pressure signals as they travel from Probes 1 to 10 is attributed to the decrease in energy of the turbulent eddies traveling downstream. However, the energy decrease in RANS is more prominent due to the numerical dissipation introduced when averaging the instantaneous governing equations. Additionally, instantaneous snapshots of the Q-Criterion in the wake region are shown in Figure 32. These comparisons indicate negligible turbulent eddies in the wake region from RANS, compared to significant activity present in DES.

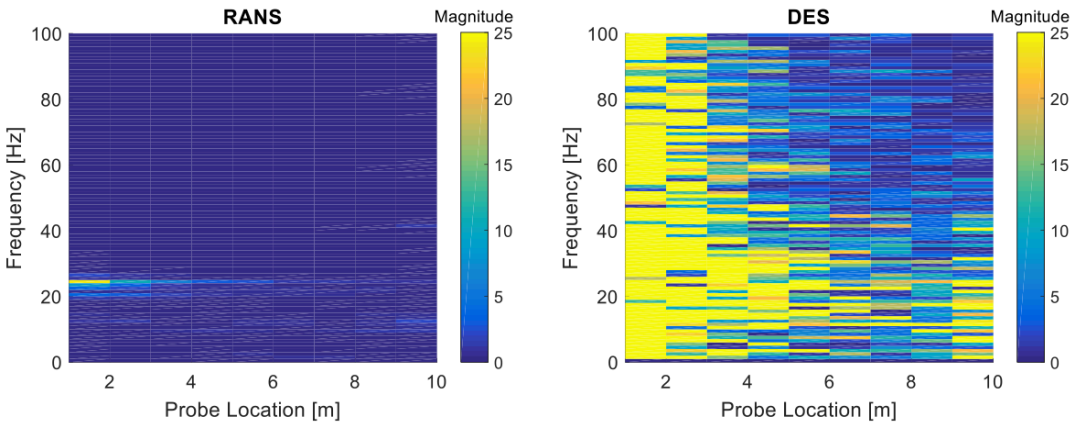

Figure 29: PSD analysis comparison of sedan - sedan configuration

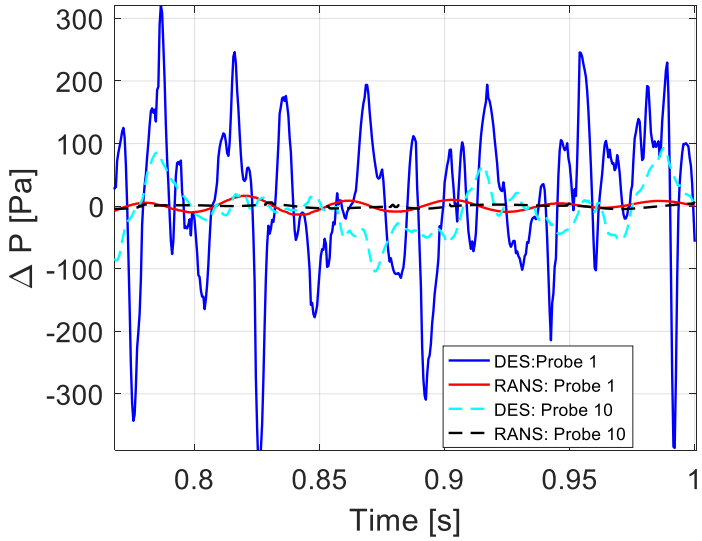

Figure 30: Fluctuating component of pressure at probes 1 and 10 (DES vs RANS)

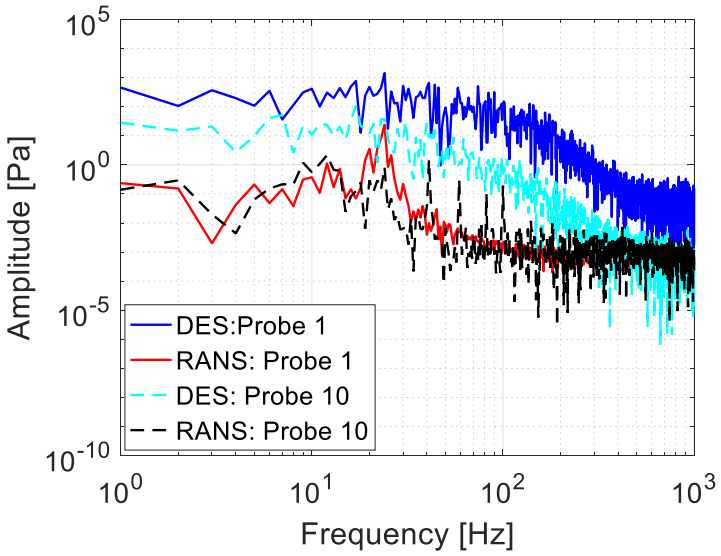

Figure 31: PSD of pressure signals at probes 1 and 10 (DES vs RANS)

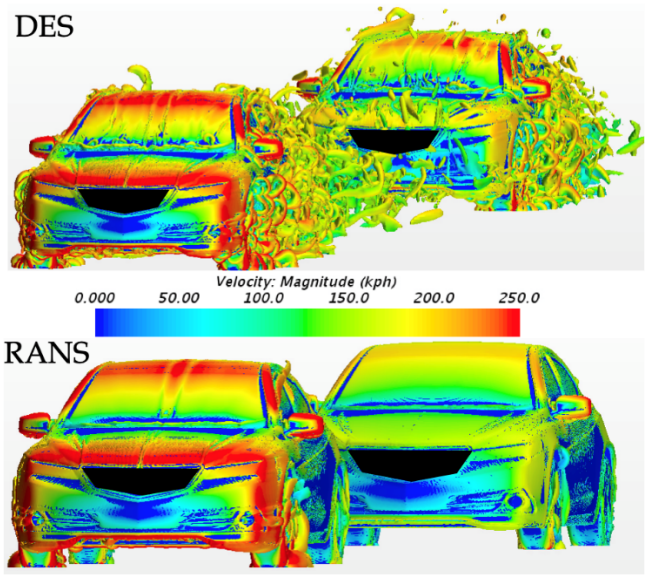

Figure 32: Sedan-sedan configuration Q-Criterion comparison

4.1.2 Structural Response

The transverse displacement of 3 discrete points on the hood is considered, illustrated in Figure 33. The displacement results are provided in Figures 34-39. As expected, RANS predicts a reduced structural response. Note that the RANS based predictions yield decaying structural response for the time interval shown. Comparatively, the DES based predictions indicate a more sustained response for the three points. As listed in Table 9, the maximum peak to peak displacements are 40-60% higher when using DES compared to RANS.

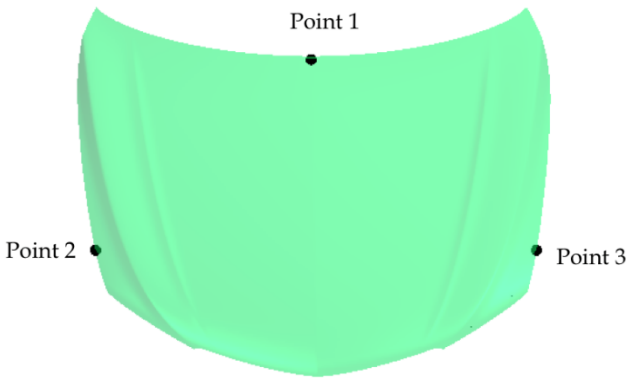

Figure 33: Displacement locations used for structural analysis of sedan hood

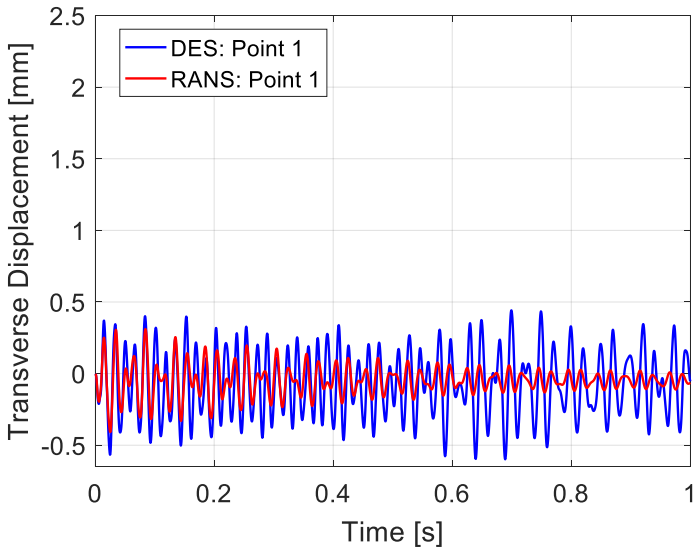

Figure 34: Transverse displacement results for sedan hood: point 1

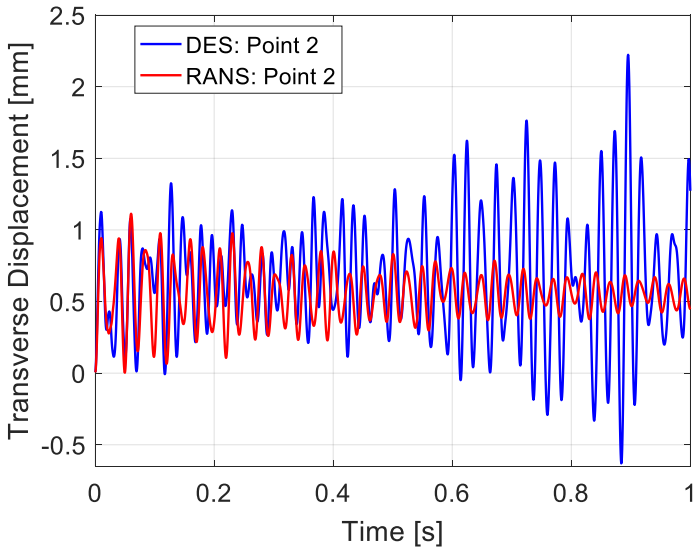

Figure 35: Transverse displacement results for sedan hood: point 2

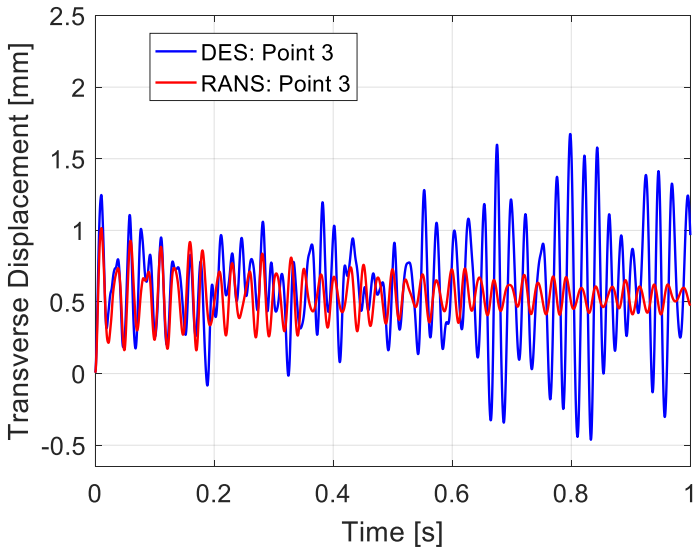

Figure 36: Transverse displacement results for sedan hood: point 2

Table 9: Maximum peak to peak displacement comparison of sedan hood

Maximum Peak to Peak Transverse Displacement			
Location	RANS (mm)	DES (mm)	% Difference
Point 1	0.61	1.04	41.35
Point 2	1.15	2.85	59.65
Point 3	1.020	2.12	51.89

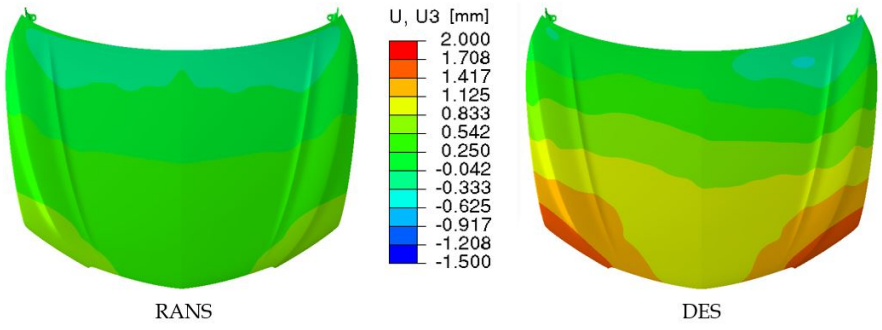

Figure 37: Instantaneous transverse displacement comparison of sedan hood: time 1

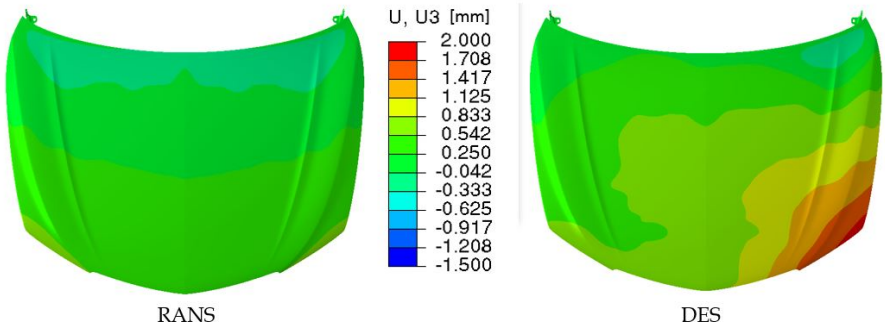

Figure 38: Instantaneous transverse displacement comparison of sedan hood: time 2

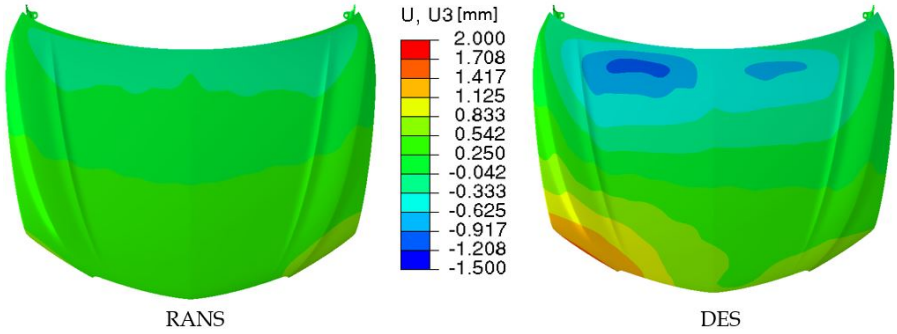

Figure 39: Instantaneous transverse displacement comparison of sedan hood: time 3

PSD analysis of the displacement for points 1-3 are shown in Figures 40-42. Point 1 oscillates at dominant frequencies of 42 and 59 Hz. These two frequencies correspond to the first and second bending modes of the hood, as shown in Figures 43 a) and 43 c), respectively. Similarly, points 2 and 3 oscillate at 42 and 59 Hz. Note that only DES captures a third frequency of 48 Hz, while RANS fails to capture it. This frequency corresponds to the first torsional mode of the hood, as shown in figure 43 b). The excitation of the torsional mode leads to increased displacements of points 2 and 3 and it is presumably due to increased span-wise variation introduced by the DES prediction.

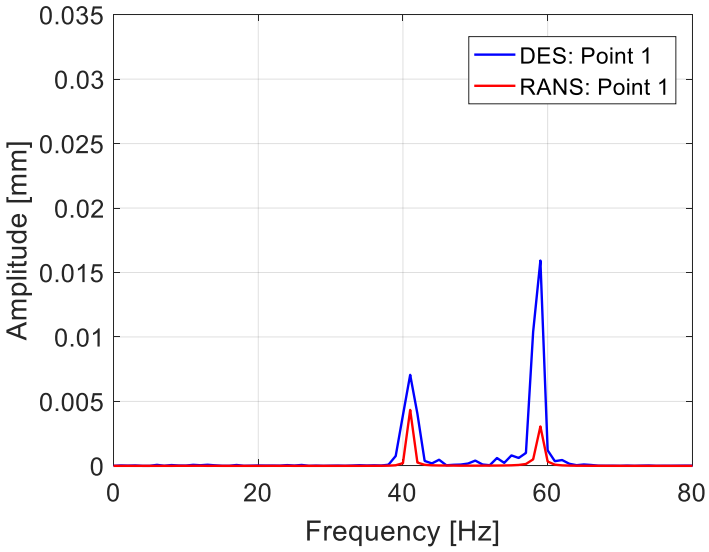

Figure 40: PSD analysis of transverse displacement of sedan hood: point 1

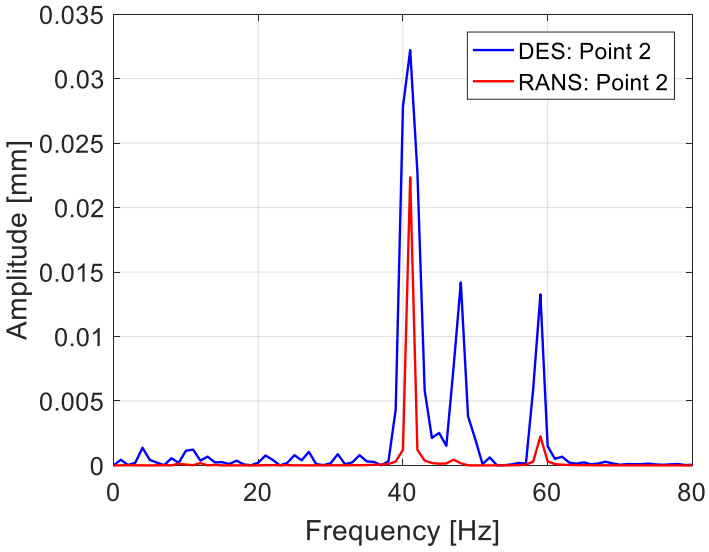

Figure 41: PSD analysis of transverse displacement of sedan hood: point 2

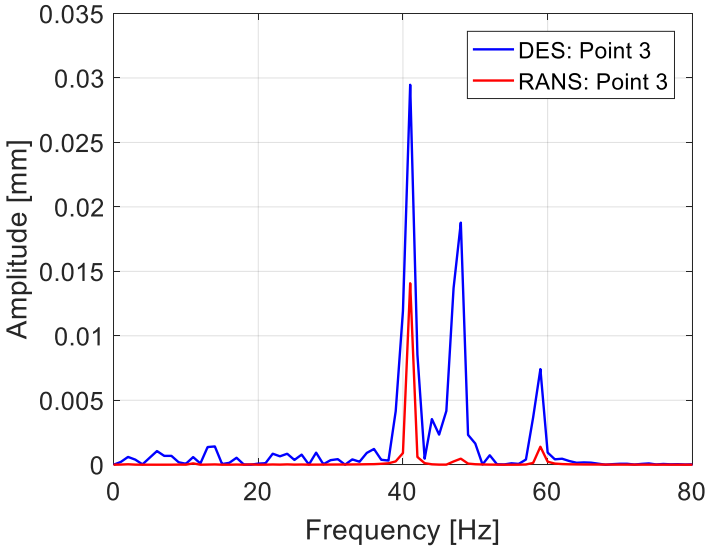

Figure 42: PSD analysis of transverse displacement of sedan hood: point 3

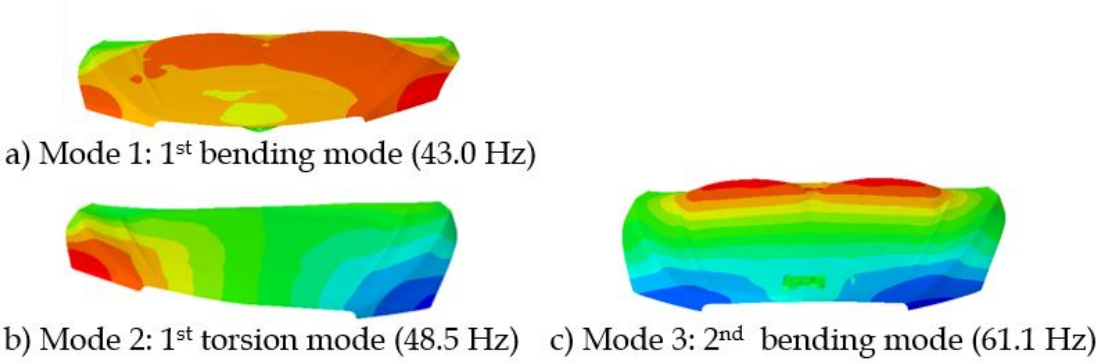

Figure 43: Natural modes 1-3 of sedan hood

4.2 Sedan – SUV Configuration

A vehicle with a more flexible hood is considered to better understand the sensitivity of automobile hoods to increased levels of turbulence in the wake yielded by DES. Similar to the previous case, force and pressure coefficients, frequency content in the flow, and the hood structural response are taken into consideration. Fully coupled simulations for this configuration are carried out at the same speed as the previous case for 0.25 seconds.

4.2.1 Comparisons Between RANS and DES Flow Solutions

As expected, the DES based predictions yield larger peak loads on the hood, shown in Figure 44. Comparisons of mean and standard deviation of the hood lift coefficient are listed in Table 10. Consistent with the results from the sedan-sedan case, though there is relatively close agreement in mean hood lift coefficient values, there is an order of magnitude difference in the standard deviation.

Table 10 Sedan -SUV Mean C_L and standard deviation

	Mean C_L	Standard Deviation C_L
DES	0.0581	0.0128
RANS	0.0498	0.00308

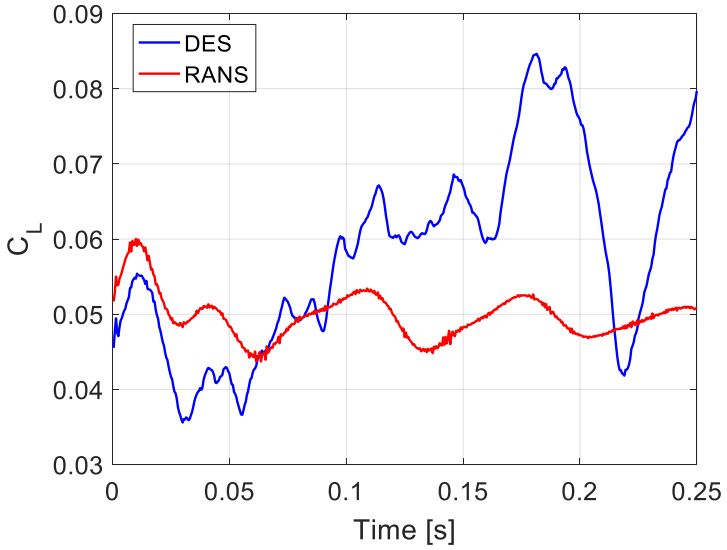

Figure 44: Time history comparison of SUV hood lift coefficient

In order to localize the areas where the pressures differ the most, time averaged pressure coefficients are taken at discrete pressure locations, presented in Figures 45-48. The high pressure followed by a steep drop at the leading edge of the hood are attributed to the steep curvature of the hood geometry in that region, where the flow experiences a rapid change of direction, resulting in flow separation. As observed in the sedan-sedan case, DES predicts larger pressures towards the leading and trailing edge, respectively, resulting in larger loads. Note that the differences between RANS and DES in the time averaged pressure coefficient distributions on this hood are larger in comparison to the similarities that are observed in the time averaged pressure coefficient distributions on the sedan hood.

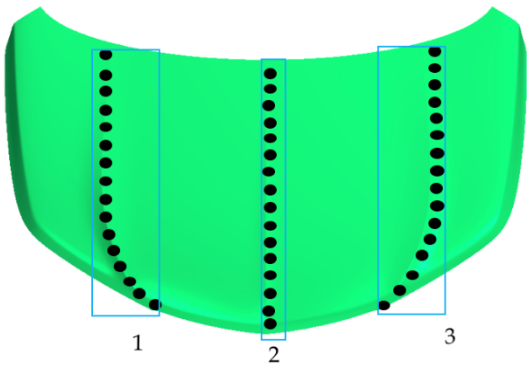

Figure 45: Discrete pressure locations for SUV hood: strips 1-3

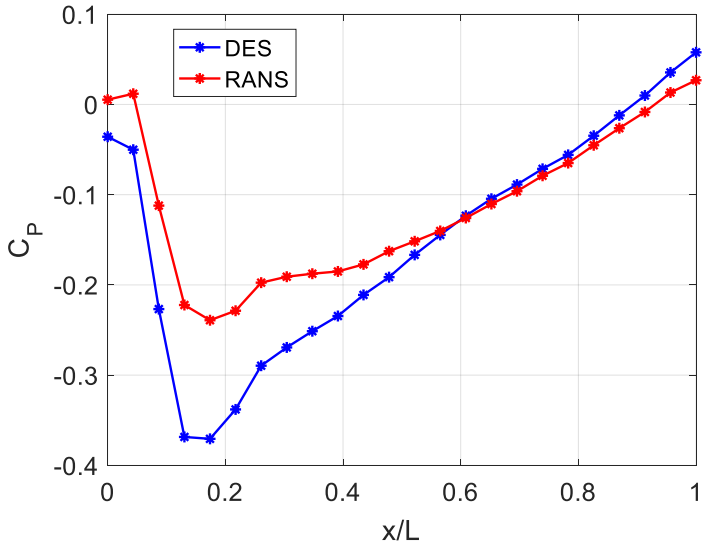

Figure 46: Time averaged pressure coefficient distribution comparison for SUV hood: strip 1

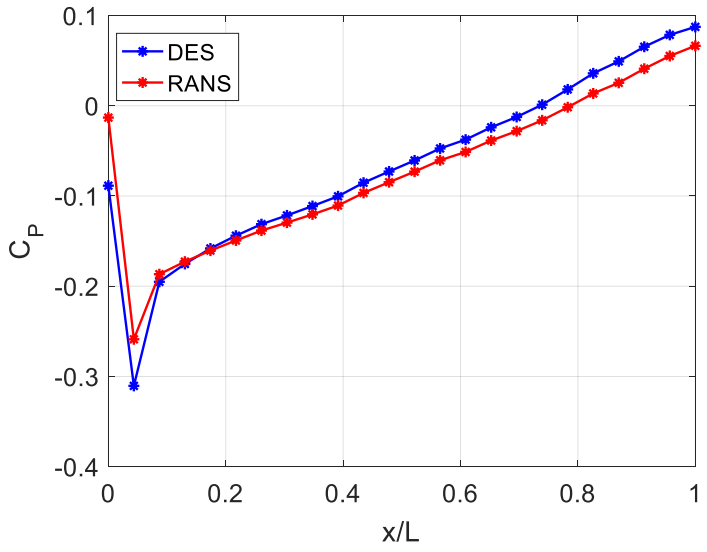

Figure 47: Time averaged pressure coefficient distribution comparison for SUV hood: strip 2

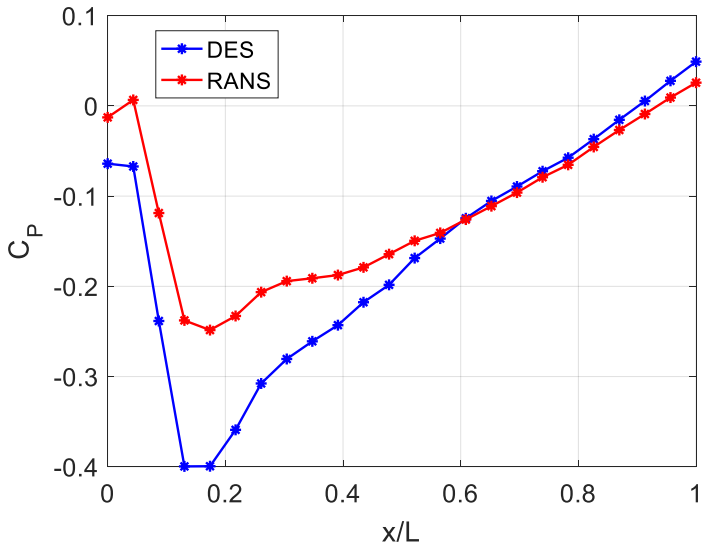

Figure 48: Time averaged pressure coefficient distribution comparison for SUV hood: strip 2

The static pressure probes that are used to carry out the frequency content analysis of this configuration are illustrated in Figure 49. Results for PSD analysis of the flow are presented in Figure 50. The dominant frequencies follow the trend that was observed in the sedan-sedan case, with dominant frequencies that convect from leading to preceding vehicle in the 10-20 Hz range for RANS and 0-40 Hz for the DES prediction. As noted earlier, the pressure fluctuation in the immediate wake of the leading vehicle predicted by RANS is significantly reduced compared to the pressure fluctuation at the last probe predicted by DES. Additionally, the instantaneous Q-Criterion snapshots, shown in Figure 51, indicate the negligible existence of turbulent eddies in the wake region from RANS, while DES predicts significant presence of turbulent eddies.

Figure 49: Static pressure probes between vehicles (sedan - SUV)

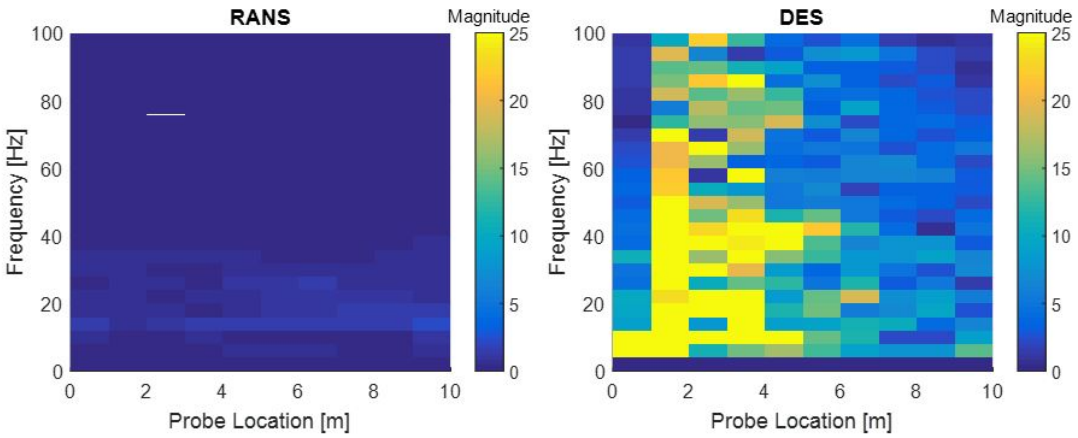

Figure 50: PSD analysis comparison of sedan –SUV configuration

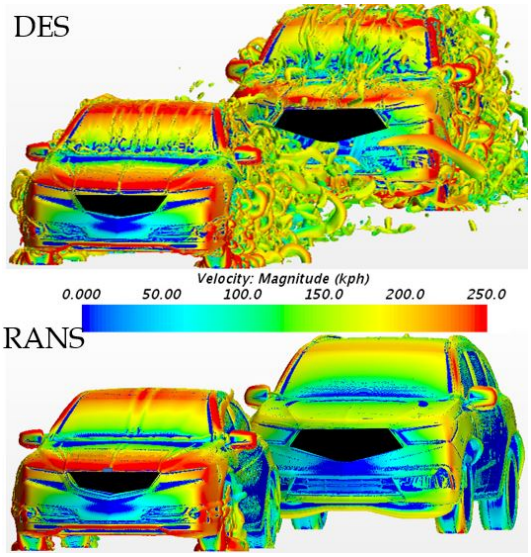

Figure 51: Sedan-SUV configuration Q-criterion comparison

4.2.2 Structural Response

The transverse displacement of 3 discrete points on the hood is considered, as illustrated in Figure 52. The displacement results are provided in Figures 53-55. Similarly, Figures 56-58 present instantaneous displacement fields at three different instances. As expected, RANS predicts a reduced structural response. For the discrete points and time interval shown, the RANS based predictions indicate a reduced vibratory response compared to the DES prediction. As listed in Table 11, the maximum peak to peak displacements are 17 - 71% higher when using DES. Consistent with the free vibration and static analyses, the magnitudes of displacement for this specific hood are considerably larger than the sedan hood. Note that the differences between RANS and DES based predictions for this configuration are increased compared to those of the sedan hood. This indicates that as the hood becomes more flexible, it becomes even more sensitive to the increased turbulence levels yielded by DES.

PSD analysis for points 1-3 are shown in Figures 59-61. All three points indicate a dominant frequency of oscillation of 12 Hz, which is near the first bending mode of this hood, as shown in Figure 62. This suggests the high participation of this mode in the vibratory response. Note that it is uncertain whether these oscillations could grow or decay in time and if higher modes could be excited. To investigate this further, a longer time response should be recorded as a future step.

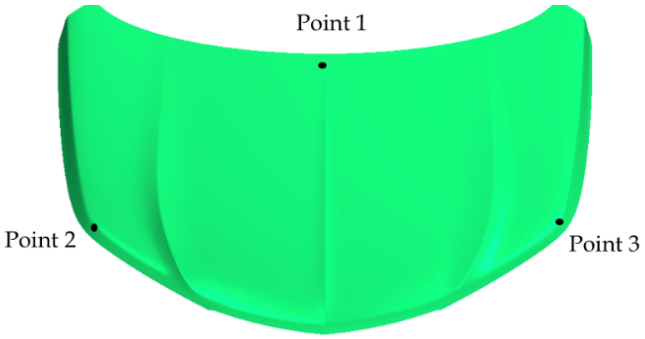

Figure 52: Displacement locations used for structural analysis of SUV hood

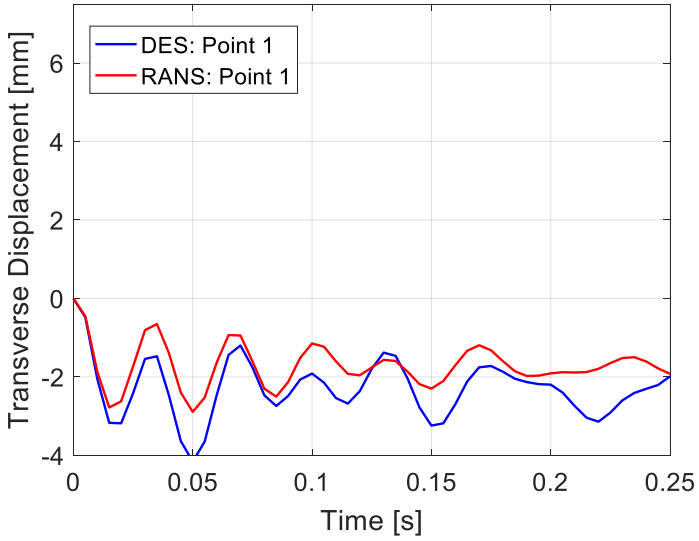

Figure 53: Transverse displacement results for SUV hood: point 1

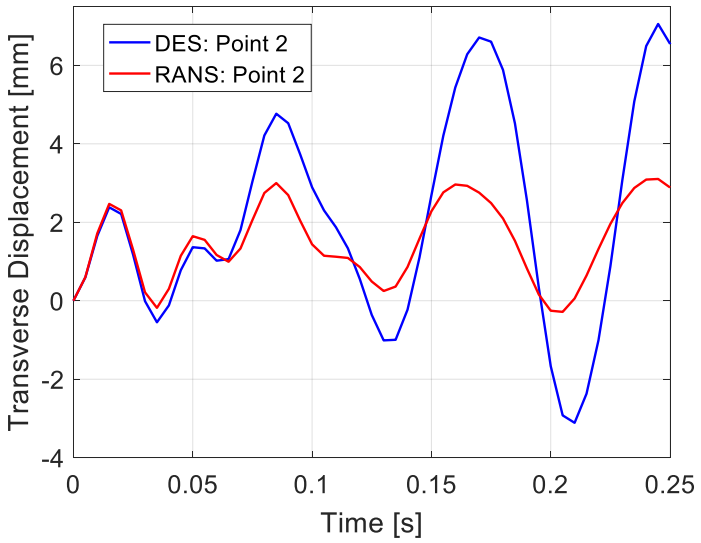

Figure 54: Transverse displacement results for SUV hood: point 2

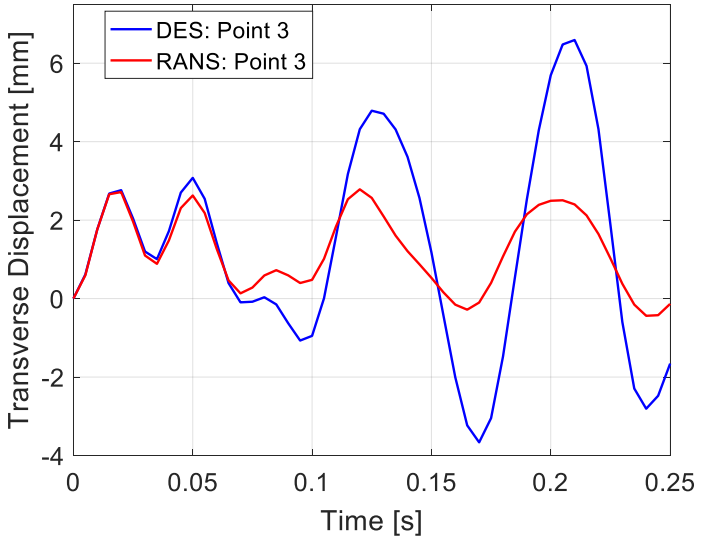

Figure 55: SUV Hood Transverse Displacement Results: Point 3

Table 11: SUV hood maximum peak to peak displacement comparison

Maximum Peak to Peak Transverse Displacement			
Location	RANS (mm)	DES (mm)	% Difference
Point 1	2.23	2.69	17.10
Point 2	3.66	10.1	63.76
Point 3	2.940	10.14	71.01

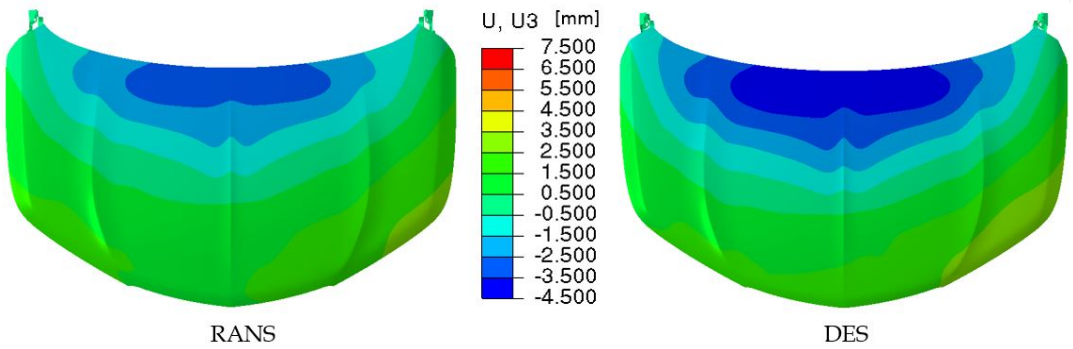

Figure 56: Instantaneous transverse displacement comparison of SUV hood: time 1

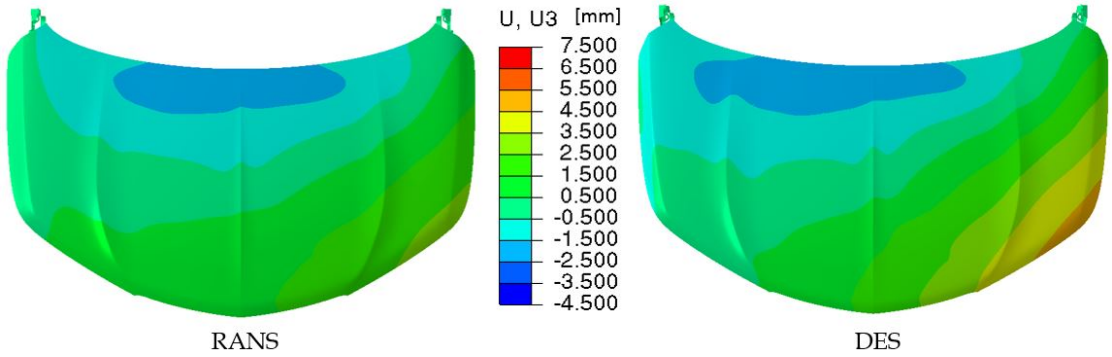

Figure 57: Instantaneous transverse displacement comparison of SUV hood: time 2

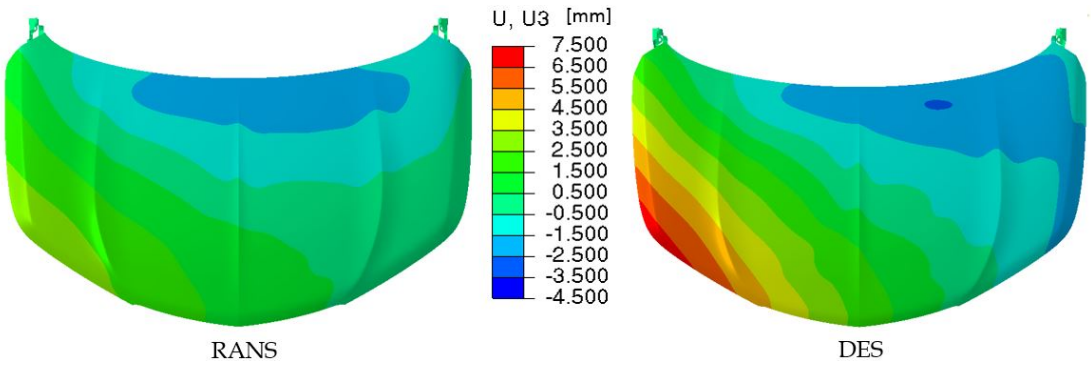

Figure 58: Instantaneous transverse displacement comparison of SUV hood: time 3

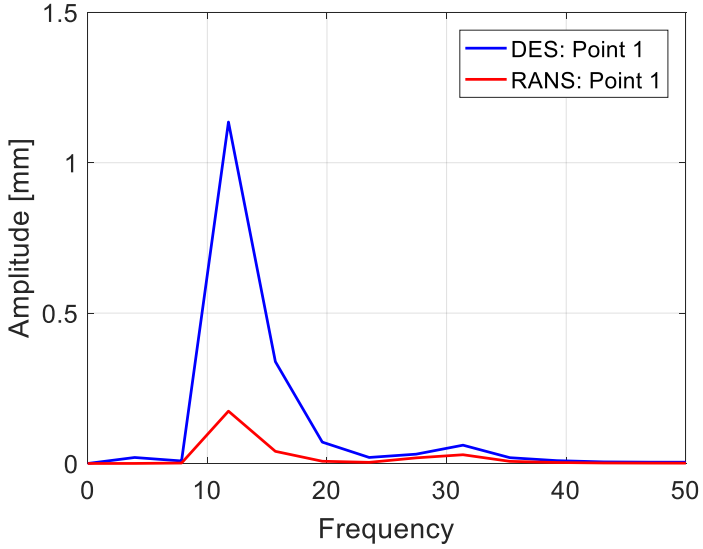

Figure 59: PSD analysis of transverse displacement of SUV hood: point 1

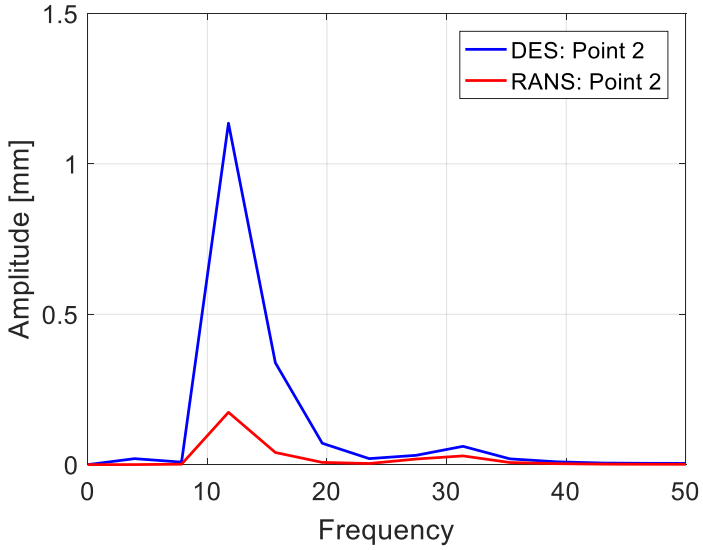

Figure 60: PSD analysis of transverse displacement of SUV hood: point 2

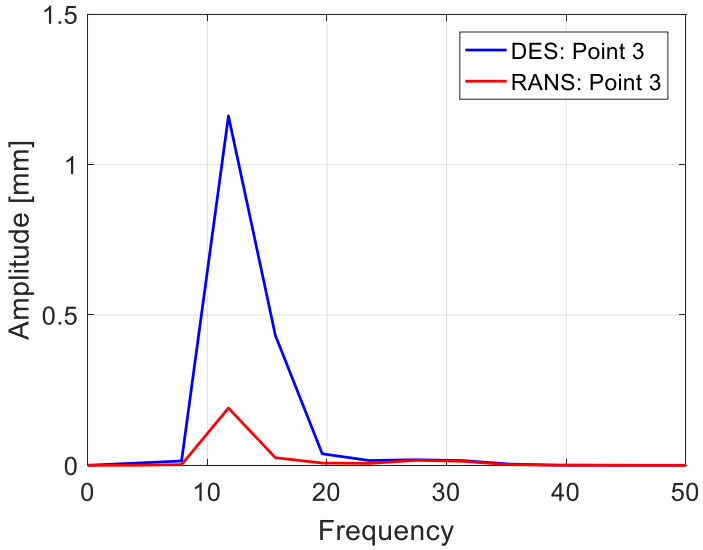

Figure 61: PSD analysis of transverse displacement of SUV hood: point 3

Figure 62: First natural mode of SUV hood

4.3 Degree of Aeroelastic Coupling

The degree of aeroelastic coupling is assessed by comparing lift coefficient time histories, pressure coefficient distributions, and mean force coefficients for both rigid and flexible configurations. This is important to determine if aeroelastic simulations are required for accurate computation of the wake-induced loads. A simpler approach may be possible where the loads are computed from a rigid configuration, and subsequently applied to the structural model to assess the structural response. Lastly, a comparison of the computational cost between rigid CFD and fully coupled FSI simulations is presented.

4.3.1 Sedan – Sedan

Results for this configuration are provided in Figures 63-68 and Table 12. In both RANS and DES, small shifts in amplitude and phase of the force coefficients are observed. This suggest that the hood deformation has a relatively small impact on the flow patterns over the hood. It can be seen that the discrete pressure distributions over strips 1-5 are almost identical, except for the DES predictions in a small portion on the leading edge area. In

terms of mean force coefficients, the differences between FSI and rigid solutions are relatively small. Note that these results are not sufficient to determine the level of fluid-structural coupling. To assess this further, an uncoupled coupled analysis should be performed to compare the transient displacement field of the hood.

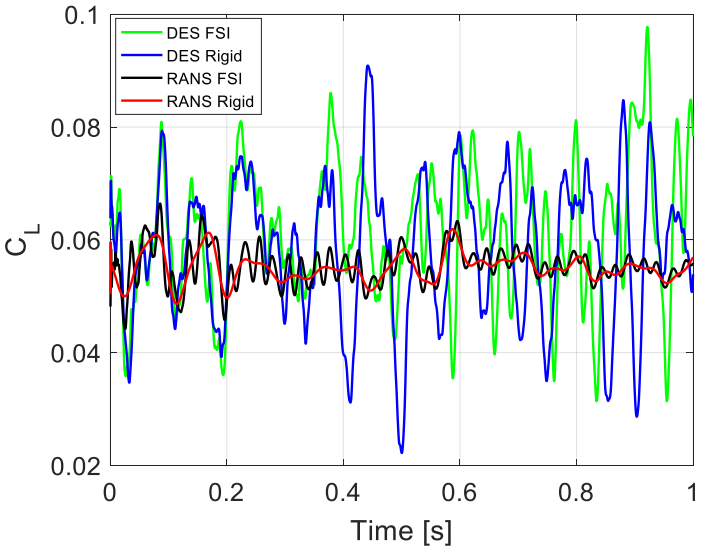

Figure 63: Time history comparison of sedan hood lift coefficient (rigid vs. FSI)

Table 12: Comparision of mean lift coefficient of sedan hood (rigid vs. FSI)

Mean C_L			
	FSI	Rigid	%Difference
DES	0.0614	0.0585	4.72
RANS	0.0554	0.0550	0.73

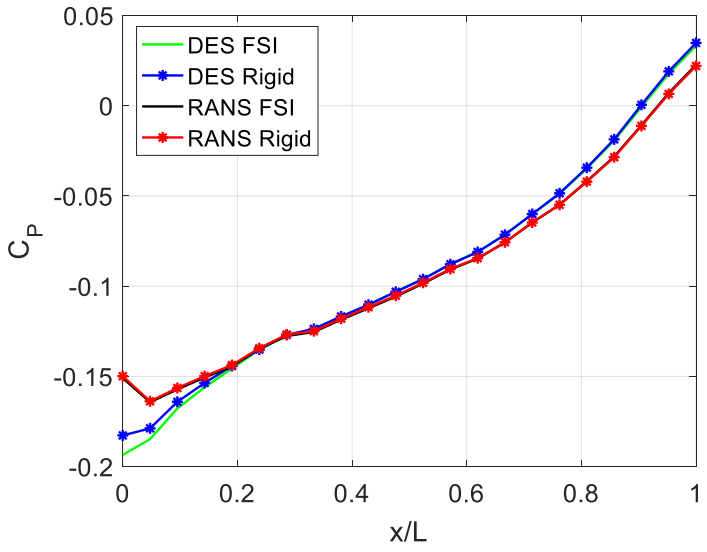

Figure 64: Time averaged pressure coefficient distribution comparison for sedan hood: strip 1 (rigid vs. FSI)

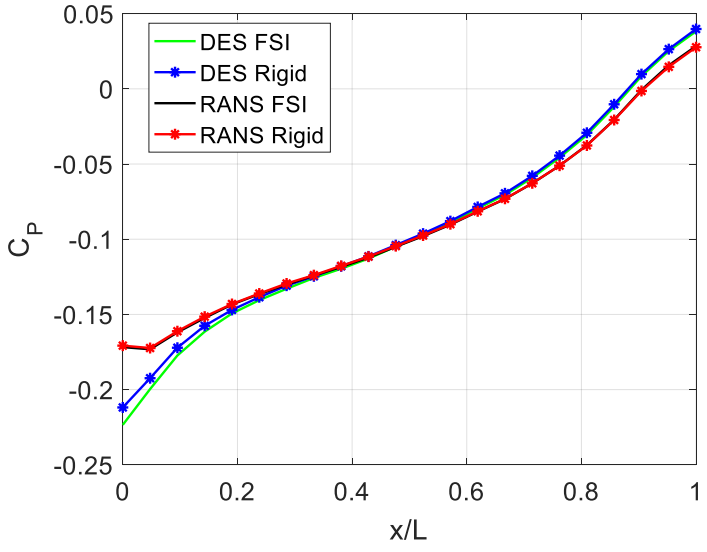

Figure 65: Time averaged pressure coefficient distribution comparison for sedan hood: strip 2 (rigid vs. FSI)

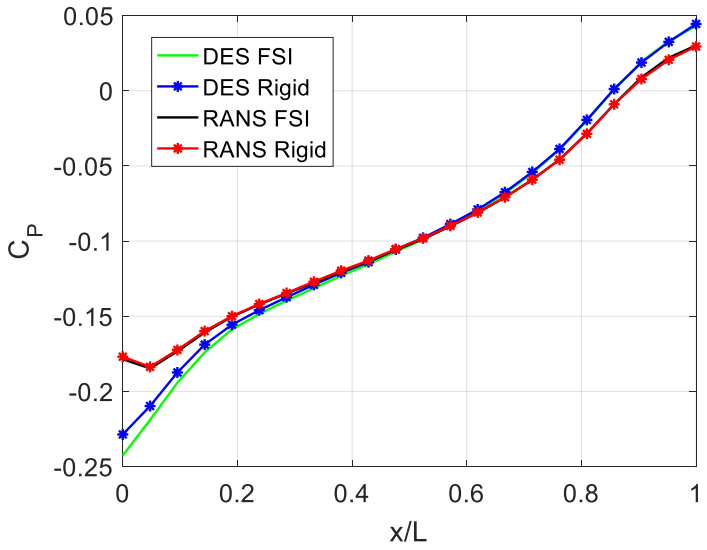

Figure 66: Time averaged pressure coefficient distribution comparison for sedan hood: strip 3 (rigid vs. FSI)

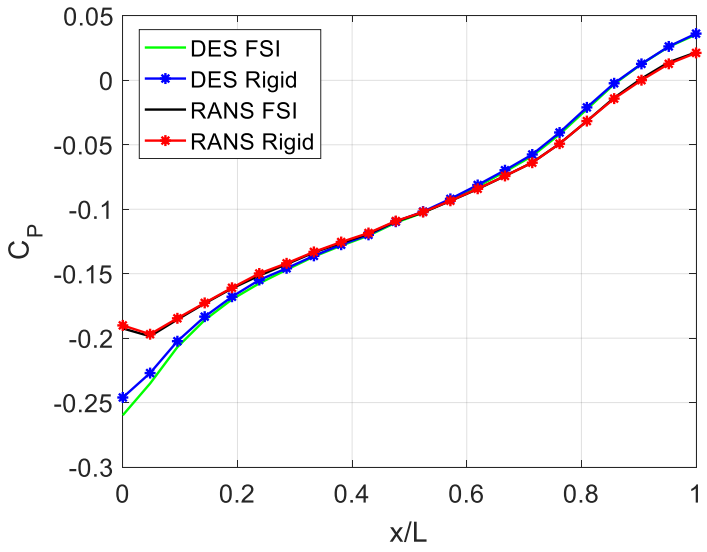

Figure 67: Time averaged pressure coefficient distribution comparison for sedan hood: strip 4 (rigid vs. FSI)

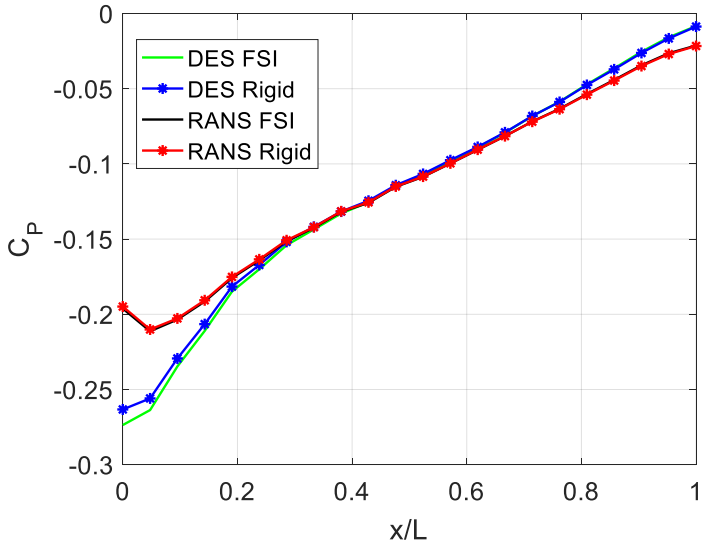

Figure 68: Time averaged pressure coefficient distribution comparison for sedan hood: strip 5 (rigid vs. FSI)

4.3.2 Sedan –SUV

Results for this configuration are shown in Figures 69-72 and Table 13. Overall, the lift force on the hood does not change substantially, except for mild phase shifts, especially in the DES solutions. The time averaged pressure coefficients over strips 1-3 yielded by both rigid CFD and FSI are almost identical. This suggests that there is no strong aeroelastric coupling on the time period over which the simulations were run. However, longer time responses should be recorded as well as an uncoupled analysis to confirm the aeroelastic coupling of this configuration.

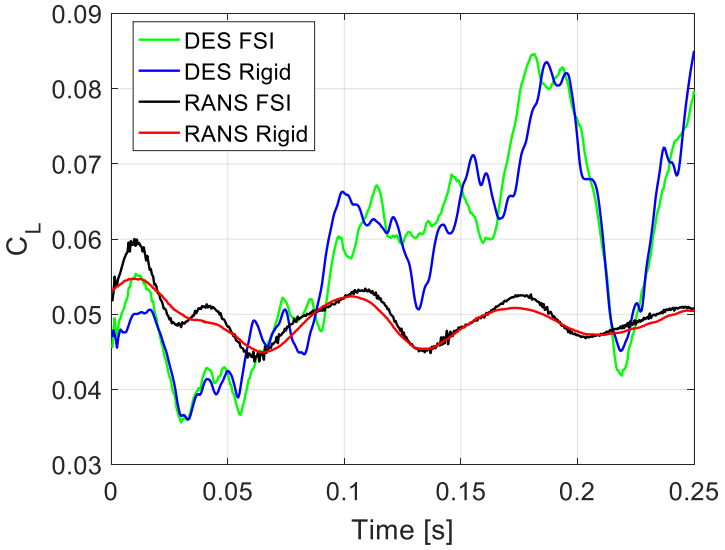

Figure 69: Time history comparison of SUV hood lift coefficient (rigid vs. FSI)

Table 13: Comparision of mean lift coefficient of SUV hood (rigid vs. FSI)

Mean C_L			
	Rigid	FSI	%Difference
DES	0.0578	0.0581	0.52
RANS	0.0492	0.0498	1.22

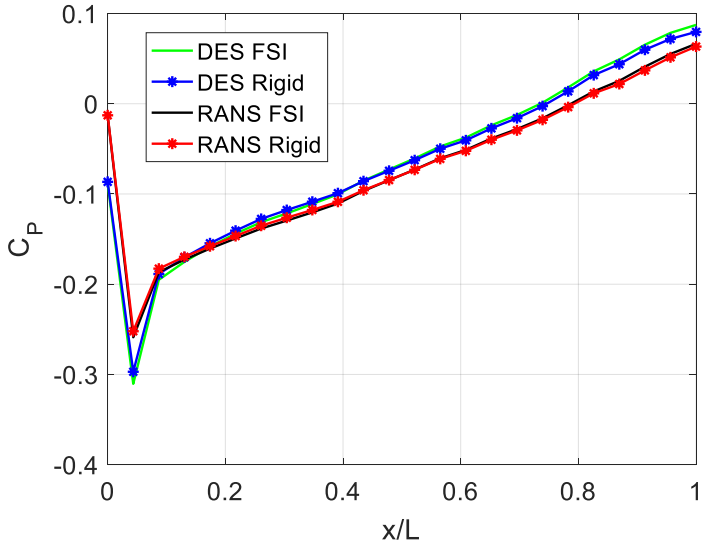

Figure 70: Time averaged pressure coefficient distribution comparison for SUV hood: strip 1 (rigid vs. FSI)

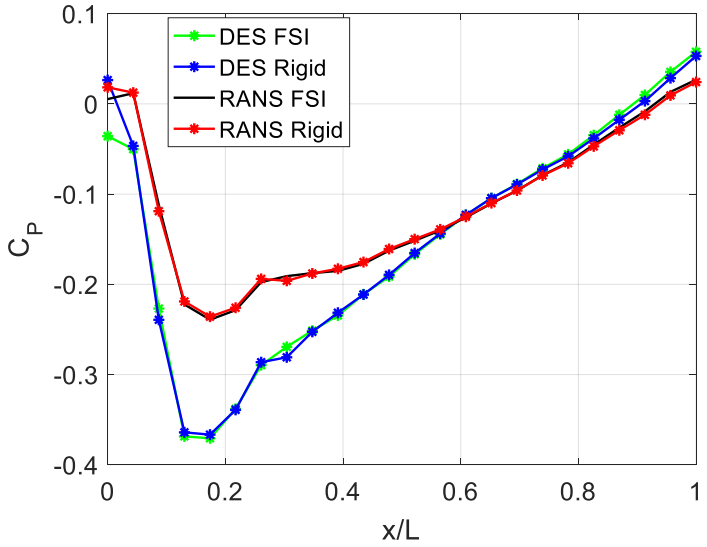

Figure 71: Time averaged pressure coefficient distribution comparison for SUV hood: strip 2 (rigid vs. FSI)

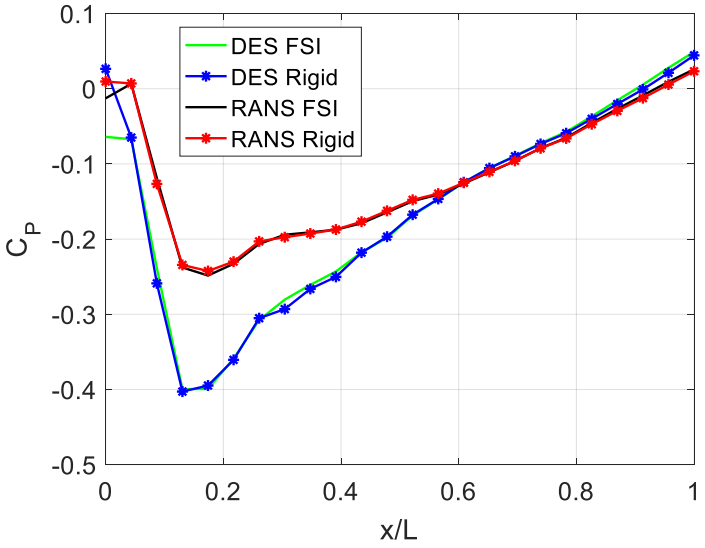

Figure 72: Time averaged pressure coefficient distribution comparison for SUV hood: strip 3 (rigid vs. FSI)

4.4 Computational Cost

In this section, a comparison of the computational cost between rigid CFD and fully coupled FSI simulations is presented in Table 14. The computational time of an FSI simulation is at least a factor of approximately 2.3 times the cost of a rigid CFD case. This increase in computational cost is due the additional time taken to perform the structural dynamics calculations as well as the mapping of boundary conditions between the solvers at every coupling time step. Note that the simulation times of the sedan – SUV configurations are scaled to 1 second for consistent comparison purposes. The increased computational costs of the sedan – SUV cases are attributed to the higher cell and element counts of the fluid and structural models, lower number of CPU cores, and slower

convergence performance of that specific case. Furthermore, note that the computational time of DES only increases by a factor of 1.3 times the cost of RANS predictions. These observations, along with the results presented in previous sections, suggest that DES comes at a reasonable computational cost, while providing significant increases in flow fidelity that impact the structural response of the hood.

Table 14: Comparison of computational time between rigid CFD and FSI simulations

Configuration		Simulation time (s)	CPU Cores	Computational Time (hr)	
				RANS	DES
Sedan - Sedan	CFD (Rigid)	1	256	39	54
	FSI	1	256	109	122
Sedan - SUV	CFD (Rigid)	1	256	51	67
	FSI	1	188	250	252

Chapter 5: Concluding Remarks

Automobile hood design is a challenging task. Several objectives in hood design lead to increased compliance, which raises the potential for adverse aeroelastic interactions. Thus, CFSI plays an important role in the design and analysis of automobiles by reducing the experimental and prototyping costs, broadening the design space and shortening the design cycle.

A CFSI framework is used to predict the aeroelastic response of hoods on a sedan and SUV trailing a sedan vehicle. Two different turbulence solvers (RANS and DES) are considered to assess the sensitivity of the structural response to the fluid modeling fidelity. Comparisons are made in terms of transient forces on the hood, pressure distributions, spectral content of the flow, vibratory hood response, peak to peak displacements, and spectral content of the structural response.

5.1 Principal Conclusions

There are several conclusions regarding the differences in turbulence modeling approaches (RANS vs. DES) and their impact on the structural response prediction of automobile hoods in high speed and turbulence conditions. As expected, RANS turbulence solvers exhibit suppression of vortex shedding behavior in the wake of a leading vehicle, while DES turbulence solvers show higher turbulence levels in the flow. Dominant vortex shedding frequencies in the 20-30 Hz range that quickly dissipate as they travel from the leading to trailing vehicle are observed in the RANS predictions. Comparatively, a stronger and much wider frequency broad band is observed in DES.

Additionally, while there is close agreement in terms of time averaged hood lift coefficient between RANS and DES, there is an order of magnitude difference in the standard deviation. This is reflected in the consistently larger peak loads on the hood predicted by DES, especially towards the leading and trailing edges or the hood.

The differences in flow solutions are consistently reflected in the wake induced hood vibration predictions. RANS flow modeling yields comparatively smaller responses to DES. Considerable differences are observed in transverse displacement predictions at the discrete points considered for this analysis. In RANS based solutions, decaying structural responses are observed, while DES based predictions exhibit more sustained responses over the time intervals shown. Furthermore, the maximum peak to peak displacement predictions by DES are between 40-60% and 17-71% higher than RANS for the sedan and SUV hood, respectively.

The longer time records for the sedan - sedan case reveal the excitation of a torsional structural mode that lead to increased displacements. Comparatively, the shorter time records for the sedan - SUV configuration do not allow for the likely excitation of other natural structural modes. This suggests that it is critical and necessary to carry out sufficiently long enough simulations to reliably assess the dynamic structural response.

Lastly, fully coupled FSI simulations require, on average, 2.3 times the cost of rigid CFD predictions. This increase is attributed to the additional time taken to solve the structural dynamics equations as well as mapping boundary conditions between the

solvers at every coupling time step. Furthermore, DES simulations (both rigid and FSI) only require a factor of 1.3 times the cost of RANS predictions, while yielding significant increases in flow fidelity that substantially impact the structural response of the hood.

5.2 Recommendations for Future Work

The results presented in this thesis only consider the numerical aeroelastic analysis of automobile hoods. A necessary next step is to perform wind tunnel or on-road experiments in order to validate these results.

Similar grid densities are used for both the sedan-sedan and sedan-SUV cases. However, different vehicle configurations exhibit different flow characteristics around the vehicles. Thus, further assessment of the grid requirements for the sedan – SUV configuration should be carried out. Similarly, longer time responses should be recorded to evaluate structural response of that vehicle more reliably.

CFSI results for full scale initial designs with simplified wheels and underbody and that neglect flow through the engine bay are presented. Next, simulations on models that include flow through the engine compartment should be considered to examine the effect of the unsteady engine bay flow on the vibratory response of the hood.

The conclusions regarding the aeroelastic coupling only considered lift and pressures on the hood from rigid CFD and FSI solutions. To further investigate the effects of surface deformation on the prediction of wake induced loads, a one-way coupled analysis should be carried out to further assess the structural response.

The vortex shedding and overall unsteady flow behavior from the preceding vehicle are unique to the specific leading vehicle geometry and speed at which these simulations were carried out. Distinct vehicle geometries at different speeds will have different vortex shedding behavior. Thus, model development for parametric studies with a few representative vehicle geometries at varying free stream velocities and turbulent intensities should be done. For instance, representative geometries of another sedan, SUV, pick-up truck, and semi-trailer truck would be interesting test cases.

Last, this study presents results for a single offset distance. Test cases with varying yaw angles and offset distances in the stream wise and span wise directions should be examined to observe the sensitivity of the hood response to the proximity and orientation of the leading vehicle.

Appendix A: Wall Y+

Accurate prediction of the flow across the boundary layer is necessary to predict realistic turbulent flows. The boundary layer can be split into three layers, the viscous sublayer, buffer layer, and log-law layer, as shown in Figure 73. The $y+$ is a non-dimensional quantity that measures the distance from the wall to the first cell center. STAR-CCM+ provides three types of wall treatments, *low - y+, high – y+,* and *all - y+*. The *low - y+* approach resolves the boundary layer without any modeling functions. This treatment requires that $y+$ values fall in the viscous sublayer $(y+ < 1)$. This requires a fine grid near the wall, resulting in large computational expenses. The *high – y+* approach uses a logarithmic function to predict the flow across the boundary layer. This approach requires that the $y+$ values fall in the log-law region ($30 < y+ < 300$). This modeling approach provides significant computational savings due to the reduction in the mesh size near the wall. The *all - y+* treatment follows a *low y+* approach for fine meshes and a *high y+* approach for coarser meshes [10]. Additionally, the *all - y+* wall treatment gives reasonable results when the $y+$ values fall in the buffer layer $(5 < y+ < 30)$. In this study, the *all - y+* approach is employed. The $y+$ distribution over the hoods and both vehicles are shown in Figures 74-76.

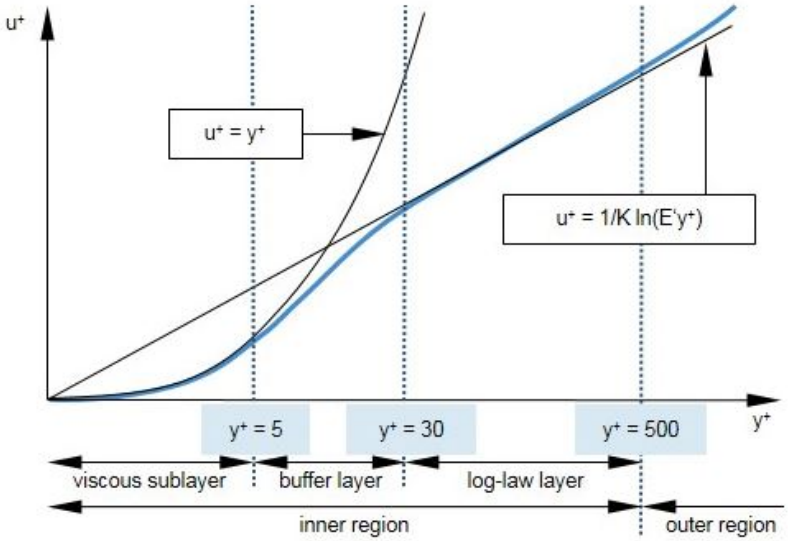

Figure 73: Boundary layer inner sublayers

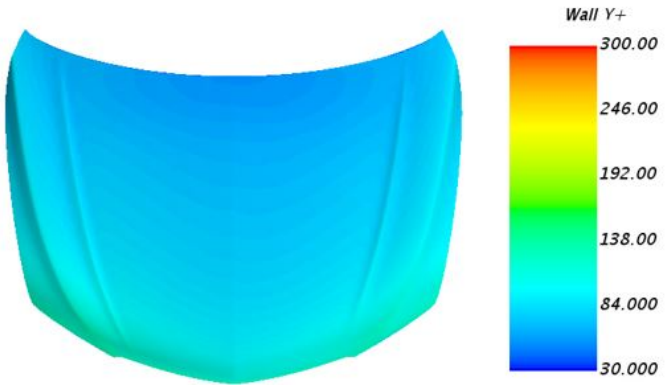

Figure 74: Sedan hood y+ distribution

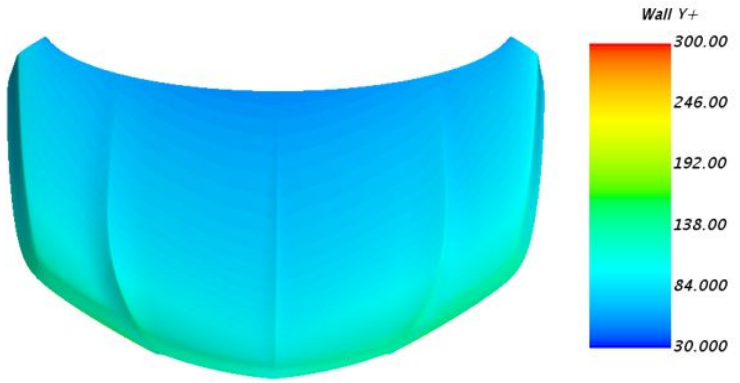

Figure 75: SUV hood y+ distribution

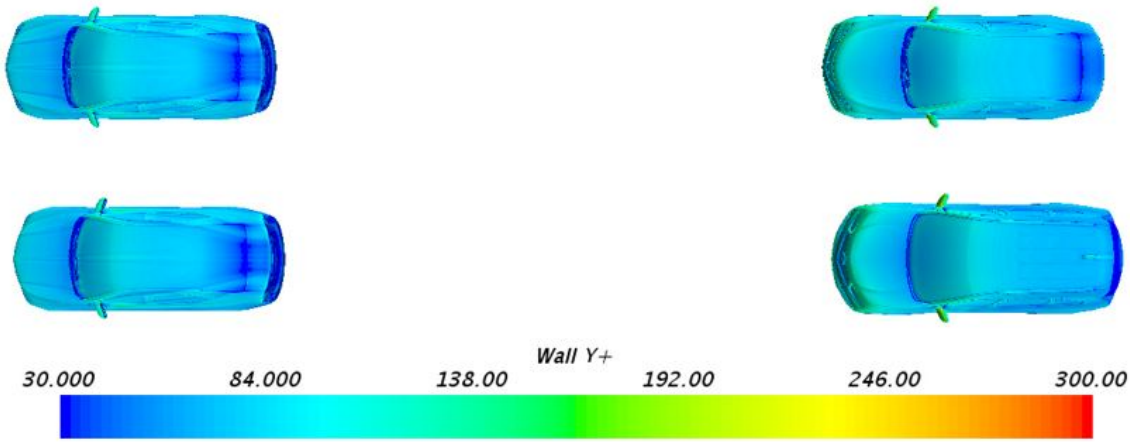

Figure 76: Sedan – sedan and sedan – SUV y+ distributions (top view)

Bibliography

[1] Pesich, J., McNamara, J., Kimbrell, A., and Kang, P., "Steady Aeroelastic Response Prediction and Validation for Automobile Hoods," *SAE Int. J. Passeng. Cars - Mech. Syst.* 11(4):2018, https://doi.org/10.4271/06-11-04-0021.

[2] Ratzel, M. and Dias, W., "Fluid - Structure Interaction Analysis and Optimization of an Automotive Component," SAE Technical Paper 2014-01-2446, 2014, https://doi.org/10.4271/2014-01-2446.

[3] Massegur, D., Quaranta, G., & Cavagna, L. (2007). An indy car rear wing is designed for aeroelastic response using multidisciplinary optimization. *ANSYS Advantage*, *1*(1), 1-50.

[4] Patil, S., Lietz, R., Woodiga, S., et al., "Fluid Structure Interaction Simulations Applied to Automotive Aerodynamics," *SAE Technical Paper 2015-01-1544*, 2015

[5] Gaylard, A., Beckett, M., Gargoloff, J., and Duncan, B., "CFD-based Modelling of Flow Conditions Capable of Inducing Hood Flutter," *SAE Technical Paper 2010-01-1011*, 2010.

[6] Gupta, A., Gargoloff, J., and Duncan, B., "Response of a Prototype Truck Hood to Transient Aerodynamic Loading," *SAE Technical Paper 2009-01-1156*, 2009.

[7] Ashton, N., West, A., Lardeau, S., and Revell, A., "Assessment of RANS and DES Methods for Realistic Automotive Models." *Computers & Fluids*, vol. 128, 2016, pp. 1–15., doi:10.1016/j.compfluid.2016.01.008

[8] Guilmineau, Emmanuel, Deng, G., and Wackers, J., "Numerical Simulation with a DES Approach for Automotive Flows." *Journal of Fluids and Structures*, vol. 27, no. 5-6, 2011, pp. 807–816., doi:10.1016/j.jfluidstructs.2011.03.010.

[9] Zhiyin, Y. (2015). Large-eddy simulation: Past, present and the future. *Chinese Journal of Aeronautics, 28*(1), 11-24. doi:10.1016/j.cja.2014.12.007

[10] STAR-CCM+ User Guide, Version 13.02.009.

[11] Bazilevs, Yuri, et al. Computational Fluid-Structure Interaction: Methods and Applications. J. Wiley & Sons, 2013.

[12] Abaqus/CAE User's Guide, Version 6.13

[13] Hodges, D.H., Pierce, G. A., (2002). *Introduction to Structural Dynamics and Aeroelasticity*

[14] Makowski, F., Kim, S., "Advances in External-Aero Simulation of Ground Vehicles Using the Steady RANS Equations," *SAE Technical Paper 2000-01-0484*, 2000.